Spatial Distribution and Mobility of the Ran and the Bicoid Proteins

SPATIAL DISTRIBUTION AND MOBILITY OF

THE RAN AND THE BICOID PROTEINS

IN

LIVE SYSTEMS

By

ASMAHAN ABU-ARISH, B. SC., M. SC.

A Thesis

Submitted to the School of Graduate Studies

in Partial Fulfillment of the Requirements

for the Degree

Doctor of Philosophy

McMaster University

DOCTOR OF PHYLOSOPHY (2008)   McMaster University

(Physics and Astronomy)   Hamilton, Ontario

TITLE: Spatial Distribution and Mobility of the Ran and the

        Bicoid proteins in Live Systems

AUTHOR: Asmahan Abu-Arish

        B.Sc. (Bethlehem University)

        M.Sc. (Weismann Institute of Science)

SUPERVISOR: Dr. Cecile Fradin

NUMBER OF PAGES: xii, 89

Acknowledgments

Dedicated to Mother

Contents

To the reader

Since I worked on two separate projects towards my doctorate thesis, the arrangement of my thesis is rather unusual. The reader will find that my thesis is divided into four parts. Part 1 is dedicated to a very general introduction about the basic knowledge needed to guide you, the reader, through the rest of the thesis. Within this part, different sections focus on different fundamental aspects of Biophysics related to my work. In Part 2, I discuss my studies of the distribution and dynamics of the nuclear protein Ran in live interphase HeLa cells. This part contains a background section specific to this project, the materials and methods used for this study, experimental results, a discussion of our findings, and it ends with conclusions. Part 3 is dedicated to the study of the dynamical mechanisms responsible for the establishment of the Bcd protein concentration gradient along the anterior-posterior axis in live *Drosophila melanogaster* embryos. Again, a specific background section is included in this part, followed by the materials and methods used to perform this research, results, discussions and finally I will summarize my results to conclude this work. The last part, part 4, is rather short and contains the summary of the overall results of my work on both nuclear proteins with some emphasis on the similarities and differences in their dynamical behavior.

Abbreviations

ACF: Autocorrelation function

bcd: bicoid gene

Bcd: Bicoid protein

Dex: Dexamethasone

EGFP: Enhanced GFP

EYFP: Enhanced yellow fluorescent protein

FCS: Fluorescence correlation spectroscopy

FRAP: Fluorescence recovery after photobleaching

GFP: Green fluorescent protein

GR: Glucocorticoid Receptor

NA: Numerical aperture

NE: Nuclear envelope

NLS: Nuclear localization signal

NPC: Nuclear pore complex

NTF2: Nuclear transport factor 2

NTR: Nuclear transport receptor

Nup: Nuclear pore complex protein

N&B analysis: Number and brightness analysis

Ran: Ras-related nuclear protein

RCC1: guanine nucleotide exchange factor for Ran

RICS: Raster image correlation spectroscopy

SAD model: Stick-and-diffuse model

SDD model: Synthesis, Diffusion & Degradation model

wtRan: wild-type Ran

List of Figures

List of Tables:

Part 1   General Introduction

As the cell is the building block of a living organism, proteins are one of the basic dynamic blocks of functional biological cells, prokaryotic and eukaryotic. Proteins regulate most cellular processes, such as cell signaling [1][2], apoptosis [3][4], intracellular transport [5], cell cycle orchestration [6], gene regulatory mechanisms [7], cellular adhesion and migration [8], embryonic cell differentiation and patterning [9], and more. Thus understanding the basics of life begins by understanding protein function, one protein at a time. The localization of specific proteins to particular cellular compartments and to different cellular organelles is an indication of their function. Another indication of functionality is the different motilities a protein displays depending on its localization, as motility is an indication of eventual interactions with other macromolecules, protein complexes or cellular structures.

In the following sections of this general introduction, I start by discussing a general introduction to the process of diffusion, with diffusion in living systems being the focus of section 1.1. The newly introduced picture of the flexibility of the nuclear structure and the mobility of nuclear proteins is discussed in section 1.2. Section 1.3 is dedicated to the phenomenon of fluorescence and the characteristics of "good" fluorophores. Section 1.4 highlights the different fluorescence techniques that were used in this work to detect protein localization and motion.

1.1 Diffusion in living systems

The peculiar dance of pollen grains suspended in water observed under a simple microscope back in 1828 was the first step towards diffusive motion identification. Arguing that there is no independent life entity in pollen grains, the botanist Robert Brown reached the conclusion that this motion could not be due to internal causes. The external agents responsible for this motion were identified in 1860: the continuous thermal agitation of the solvent molecules and their constant collisions with the grains are the cause. This phenomenon was called "Brownian motion" after Brown who observed it for the first time [10]. A. Fick was the first to fully describe this motion mathematically and to derive the diffusion equation which can be solved after initial and boundary conditions' specification [10]:

$$\frac{\partial C(\vec{r},t)}{\partial t} = D\nabla^2 C(\vec{r},t) \qquad (1.1.1)$$

Where $C(r,t)$ is the three-dimensional non-uniform concentration distribution of particles undergoing diffusive motion at time t, and D is the particle specific characteristic constant of the diffusive motion, called diffusion coefficient. A detailed description of the mathematical derivation of equation (1.1.1) is out of the scope of this thesis and can be found elsewhere [10]. Considering the special case where one particle is at the origin at time $t=0$, the solution to the diffusion equation, $C(r,t)$, describes the probability this particle is found at position r at time t. The diffusion coefficient can be found to be proportionally related to the mean-square-displacement of the diffusive particle at time t as follows:

$$D = \frac{\left\langle r^2(t)\right\rangle}{2dt} \qquad (1.1.2)$$

The diffusion coefficient thus physically describes the mean-square-displacement undergone by the particle. If the particle is diffusing in 2-dimensions, as is the case for diffusion in membranes, $d=2$. In solution, the description of the 3-dimensional diffusion process requires $d=3$.

In 1905, Albert Einstein unified existing theories into a rather simple relation combining the nature of the dynamics of the microscopic solvent molecules and the final macroscopic result

of their collisions on larger molecules, the diffusion coefficient, in the following relationship (known as Stokes-Einstein formula) [10]:

$$D = \frac{kT}{6\pi\eta R} \qquad (1.1.3)$$

where T is the absolute temperature, k is the Boltzmann constant, η is the viscosity of the medium surrounding the diffusing molecules, and R is the hydrodynamic radius of the diffusing molecule.

In biological systems, proteins may reach their preferred localizations through two different dynamical processes: diffusive or directed motion. Intracellular diffusion is a predominant yet energy independent form of protein transport. Although diffusion is a slower and less efficient form of transport when compared to active transport, the small dimensions of cells and the short distances between targets ensure high efficiency within short periods. According to Eq. (1.1.2) and Eq. (1.1.3), probing diffusion allows for medium's viscosity determination, molecular size calculation as well as temperature measurements when proper controls are used.

The absolute temperature in cells is generally constant (315 K in human cells), and so the mobility of a protein is solely dependent on its size and the viscosity of the cellular medium (Eq. (1.1.3)). However both of these factors can have non-trivial dependence on several other factors in living systems. The binding of proteins to other protein complexes increases their apparent size and so reduce their diffusion coefficient. Therefore a reduction in diffusion coefficient is an indication of the protein's activity. DNA, endoplasmic reticulum (ER), mitochondria and other internal cellular structures act as obstacles in the way of freely diffusing proteins (sieving effects), reducing their mobility and changing the nature of the mobility from simple diffusion to anomalous diffusion. Transient binding of proteins to immobile cellular structures changes the nature of the protein mobility as well, resulting in a reduced apparent diffusion coefficient when compared to that of freely diffusing protein.

Isolating the factors involved in the modification of diffusion behavior as well as determining the amplitude of their effects is of great importance for the understanding of the biological functions of a protein of interest, and has been one of the challenges of the work

presented here. In order to build a clear dynamical map of the proteins under investigation, we therefore decided to employ several complementary fluorescence techniques and to analyze our experimental data with different mathematical models. As an example, when analyzing fluorescence correlation spectroscopy (FCS) data, different models were used to isolate the factors contribute to the evident dynamical slow down of the protein under investigation and as a consequence isolating the origins of possible anomalous diffusion behavior. The data was analyzed using anomalous diffusion model [11] first. To consider the possibility of protein complex formation instead, the data is analyzed using multi-component diffusion model [12]. The Stick-and-diffuse model explores the possibility of detecting transient binding of the investigated protein to immobile cellular structures such as the DNA [13]. Detailed description of the techniques and the models used will be discussed in the last section of this introduction.

1.2 Dynamics of nuclear proteins

Traditionally, the nucleus was viewed as a static structure with nuclear proteins shuttling between the nucleus and the cytoplasm through the nuclear pore complexes which span the nuclear envelope. Once in the nuclear compartment, proteins were thought to form stable multi-protein complexes and/or bind to the nuclear structure for a relatively long time for functional purposes. This view was opposite the perceived view of the cytoplasm, which was considered highly dynamic and was studied more thoroughly. Not until FRAP and FCS were employed to intensively study the actual mobility of nuclear proteins in living systems was our static view of the nucleus modified. A number of nuclear proteins have now been put under the microscope and dynamically investigated in their natural environments. Most nuclear proteins studied were found to be highly dynamic, exhibiting both free diffusion in the nucleoplasm and rapid exchange with their targets (with characteristic binding times on the order of seconds) [14-18].

The number of publications and reviews about this topic is massive, but two selective examples are presented here to highlight the role of fluorescence photobleaching (FRAP) and fluorescence correlation (FCS) techniques in uncovering the nature of nuclear proteins' mobilities.

In the year 2000, Phair et al. measured the mobility of three different nuclear proteins in the nucleus of living cells using photobleaching techniques [15]. The nucleosomal binding protein HMG-17 (involved in transcription), the pre-mRNA splicing factor SF2/ASF and the rRNA processing protein fibrillarin have distinctive nuclear localizations and are involved in diverse nuclear processes. The authors carried out fluorescence recovery after photobleaching (FRAP, see section 1.4.3 for details on this technique) experiments to probe the mobility of GFP-fusion versions of the proteins which were transiently expressed in BHK and in HeLa cells. Surprisingly, the recovery of the three proteins in the nucleoplasm was complete within 30 s, with a half-time of $\tau_{1/2} \sim 3$ s. The absence of immobile fractions of all proteins was reported in this study as well. The measured mobility of these proteins was significantly lower than that of GFP alone (the experiment's control) in the same compartment. The slow mobility was proposed to be due to proteins interactions and complex formations with nuclear components and not due to size effects. All three GFP-fusion proteins proved to undergo fast diffusive motion throughout

nucleus and to rapidly associate and dissociate with nuclear structures. Since functionally unrelated nuclear proteins exhibited similar mobility, the authors concluded that "high mobility is a general feature of nuclear proteins in vivo". This high mobility is suggested to be essential for proteins to find the appropriate binding partners at low energy cost, serving by that the efficiency of the complex regulatory mechanisms in the nucleus.

The glucocorticoid receptor (GR) is a transcription factor that controls a broad range of gene regulatory mechanisms. GR is localized to the cytoplasm and is known to associate with several binding partners before activation. In the presence of an activation agent like Dexamethasone (Dex), the human GRα isoform (GRα) is driven to the nucleus to associate with genomic response elements [12] and so perform its transcriptional regulatory function. The dynamics of a GFP-tagged GRα in the nucleus of living cells was investigated using both FRAP and fluorescence correlation spectroscopy (FCS, for details about the technique see section 1.4.4). FRAP demonstrated that the receptor exchanges rapidly with its chromosomal regulatory sites in the nucleus, with half-time of $\tau_{1/2} \sim 5$ s [16]. The high sensitivity of FCS on the other hand demonstrated that this receptor undergoes two different dynamics in the nucleus: fast diffusive motion (D$\sim$14 μm^2/s) and a significantly slower dynamical process that is related to dimerization, complex formation or/and rapid transient binding to the DNA (D$\sim$0.3 μm^2/s, after activation) [12]. In this study, three different mutants of the receptor were constructed to elucidate the slow component and investigate its origins. The diffusive motion of the mutants was not affected after activation but the slow-moving GRα was found to be affected by DNA binding and complex formation rather than dimerization. FCS and FRAP are complementary techniques that clarified the highly dynamic mechanisms of this biomolecule in its natural environment.

1.3 Fluorescence and fluorescent molecules

Molecules are said to fluoresce when they absorb light photons with a specific wavelength and re-emit photons with a longer wavelength. What happens at the level of the molecule is that the absorption of the photon excites the molecule from its ground state to a higher energy excited state. The molecule then decays back to its original state, and emits another photon in the process. One might think that the absorbed and emitted photons should be of equal energy (and therefore wavelength), but since some of the excitation energy is dissipated through non-radiative electronic transitions between vibrational levels the emitted photon has in fact a longer wavelength than the absorbed photon. Because of the existence of multiple vibrational levels within the ground state and the first excited state, fluorescence absorption and fluorescence emission spectra are not sharply peaked at a single wavelength, but rather encompass a range of different wavelengths centered on the most populated excitation/emission transitions. The exact shape of the excitation/emission spectra depends on the fluorophore's chemical composition. The difference in wavelength between the absorption and emission spectra maxima is called Stokes shift [19].

There are several factors that restrict the number of molecules that can fall under the "good fluorophore" category, with respect to their usefulness for fluorescence experiments in live cells. First, since efficient fluorescence detection relies on the ability to separate fluorescence excitation from fluorescence emission (which is usually done with the help of a dichroic mirror and a notch filter), fluorophores with a high Stokes shift are potential candidates. Fluorescence quantum yield, which is defined as the ratio of the number of fluorescence photons emitted to the number of photons absorbed by the molecule, is another important factor. A fluorescent molecule with high quantum yield is required for efficient detection and for successful distinction between the fluorescence signal and background auto-fluorescence signal often present in cells. The lack of detectors that can efficiently detect photons with wavelength in the infrared region limit our choices of fluorophores. In biological systems, heating effects and covalent bond breakage are good reasons to avoid using fluorophores excited by infrared and ultraviolet radiation, respectively. Thus the commonly used fluorophores for biological

applications are those excited and emitting through the visible light spectrum, preferably with a high quantum yield and large Stokes shift [19].

Organic fluorophores (dyes) have been available for use since very early on. Although successful for in vitro investigations, these dyes suffer severe shortcomings when used to probe organelle or protein distribution and dynamics in living systems. Dyes used to chemically label cellular proteins of interest and then inject them in live cells exhibited different levels of toxicity [20]. When they are excited, dyes can produce toxic radicals and thus generate reactive oxygen species. This can alter the regular cellular machinery and so the actual distribution and function of the protein under investigation. Since dyes are chemically attached to proteins of interest, the existence of free dye together with labeled proteins is a likely scenario through insufficient purification or through dissociation of the dye after injection in live systems increasing the background signal to a point that makes it hard to isolate the much needed signal for protein investigated.

The extraction of the naturally occurring green fluorescent protein (GFP) from the jellyfish *Aequorea victoria* in 1962, and the use of it as a fluorescent marker instead of dyes revolutionized our understanding of protein distribution, dynamics and function in live biological systems [21]. The chromophore of GFP is found to be a part of the peptide's backbone but separated from environmental conditions by being localized to the center of the unique β-barrel tertiary structure of the GFP protein. The ability to genetically tag cellular proteins with GFP without altering their function is one of GFP's great advantages, allowing for *in vivo* biological processes characterization. No dissociation is expected as that of dyes and so accurate dynamical measurements can be achieved with a minimal background signal. By virtue of its seclusion from the cellular environment, the GFP chromophore is expected to be less toxic than that of organic dyes, an added advantage to the list. Since the chromophore is protected inside the tertiary structure of the GFP protein, fluorescence quenchers have little or no effect on GFP fluorescence. The high quantum yield (ϕ=0.8) of GFP is just another attraction. The purified wild-type recombinant GFP showed no significant difference in its stability properties or quantum yield when compared to that of natural GFP purified from *A. victoria*. Since the discovery of the GFP, many mutants of the wild-type GFP were introduced resulting in enhanced

quantum yield (Enhanced Green Fluorescent Protein, EGFP) and shifts in absorption and emission spectra (Enhanced Yellow Fluorescent Protein, EYFP, Enhanced Cyan Fluorescent Protein, ECFP). The naturally occurring wild-type GFP as well as the recombinant mutants exhibit characteristic photophysical properties, which result in fluorescence blinking [22][19][23].

It was not until recently that fluorescence was put to use for studying molecular dynamics, molecular conformational changes, protein localization, and concentration measurements in biological systems. This revolutionary advancement was paralleled with technological advancement in optics, laser production and fluorescence detectors, as well as with the discovery of the green fluorescent protein (GFP). The introduction of the concept of confocal microscopy was crucial as well. The combination of all of the above gave rise to the wide-spread use of fluorescence techniques among biologists, biochemists and biophysicists. Examples of these techniques include (but are not limited to) Fluorescence Correlation Spectroscopy (FCS) [23][12], Fluorescence Recovery after Photobleaching (FRAP) [18][24], Förster Resonance Energy Transfer (FRET) [25, 26], Fluorescence Lifetime Imaging Microscopy (FLIM) [27, 28] and Fluorescence Intensity Analysis [29]. More recently, new fluorescence analyses based on the conventional scanning confocal imaging technique emerged, such as Image Correlation Spectroscopy (ICS) [30, 31] and its several derivatives, for example Raster-Image Correlation Spectroscopy (RICS) [32-34], and molecule Number and Brightness Analysis (N&B analysis) [28, 35]. Several of these methods are detailed in section 1.4.

1.4 Fluorescence techniques

In this section we review the different fluorescence techniques that were used in the study of cellular distribution and mobility of both fluorescently tagged proteins, EYFP-Ran and Bcd-EGFP in their respective live systems.

1.4.1 Fluorescence intensity analysis

When a particle is tagged to a fluorophore, the fluorescence signal collected at a certain point in the sample using a wide-field fluorescence microscope or a scanning confocal microscope is related to the concentration of that particle. The fluorescence intensity recorded is the product of the fluorescent particle concentration and the molecular brightness (amount of fluorescence recorded per fluorophore) of the fluorophore used for tagging (the molecular brightness is in turn related to the excitation intensity, the quantum yield of the fluorophore and the efficiency of fluorescence collection and detection). Assuming that every particle is labeled with a fluorophore, and that the fluorophore molecular brightness is uniform throughout the image, fluorescence intensity should be linearly proportional to concentration. Fluorescence intensity analysis thus in principle allows the determination of a protein concentration distribution. For example it can be used to quantify the relative concentration of a protein in two different cellular compartments, simply by estimating the ratio of the fluorescence intensities measured in these different compartments. The absolute concentration of the protein, c, can be calculated only when the fluorophore's molecular brightness, B, has been measured under similar imaging conditions. In that case the fluorescence intensity, $I=c*B$.

For this study, fluorescence intensity analysis was performed on images taken with a Nikon EZ C1 scanning confocal microscope (v.1.7). For both EYFP-Ran and Bcd-EGFP, fluorescence was excited using the 488 nm radiation of an Argon ion laser with a ~5 µW power at the sample (corresponding to 0.5 kW/cm^2). An oil-immersion objective lens (Nikon 100x, NA=1.3) was used with a matching 61.5 µm diameter pinhole. A detailed description of scanning conditions used for optimized fluorescence intensity images is given in part 2. The software

ImageJ was used in this study to quantify fluorescence from images and to obtain an estimate of the corresponding standard deviations.

1.4.2 N&B analysis

Molecule number and brightness (N&B) analysis is a method that allows retrieving the average concentration and molecular brightness of fluorescent particles at each pixel of two-dimensional time-series of confocal images [28, 35]. The standard deviation from the average fluorescence intensity at each pixel is related to the detector shot noise and to the temporal fluctuations in the number of fluorescent particles at each pixel. Calculating the second moment of the distribution of fluorescence intensities for a given pixel thus gives access to both molecular brightness and average number of molecules in the confocal volume, according to the analysis originally proposed by Qian and Elson [36]. We performed N&B analysis of scanning confocal image stacks using the software SimFCS (Laboratory for Fluorescence Dynamics, Irvine, CA).

For N&B analysis, images were collected using the same laser scanning confocal microscope as for fluorescence intensity analysis (Nikon EZ C1, v.3.2) but using slightly different scanning conditions. A detailed description of the scanning conditions used for experiments with Ran is given in part 2, and for experiments with Bcd in part 3.

1.4.3 Fluorescence Recovery after Photobleaching (FRAP)

FRAP is a commonly used technique to study molecular mobility. The study of protein mobility in living systems is made possible when the protein is non-invasively tagged to the green fluorescent protein (GFP) or any of its variants. Typically, the cell of interest is first imaged using low fluorescence excitation intensity in order to determine the initial fluorescence intensity across the cell. Secondly, a small diffraction limited area of the cell is quickly and irreversibly photobleached using a high-intensity and stationary laser beam. The region selected is dependent on the fluorescent protein localization and researchers' interests. The recovery of fluorescence in the bleached area is measured using low laser power to avoid unneeded photobleaching. The recovery trace describes the redistribution of the molecules in and out of the

photobleached area. Since particles entering the photobleached area are fluorescent and those leaving are photobleached, fluorescence is expected to increase in the monitored region. This setup is referred to as Gaussian-spot FRAP. Analytical models describing the recovery process have been developed. By fitting the fluorescence recovery to one of these models, two parameters can be extracted: the average diffusion coefficient (D) and the immobility fraction of the fluorescently tagged molecule. Several variations of FRAP were later introduced, and the most commonly used at present is the so-called confocal FRAP. This variant of Gaussian-spot FRAP employs a commercial scanning confocal microscope for bleaching and monitoring the fluorescence recovery in a selected extended region (typically a few microns in diameter). Although widely available and easy to use, this scheme suffers limitations. Since photobleaching requires that we scan the region of interest at least once, much longer bleaching time is required when compared to that of the Gaussian-spot FRAP. This in return results in loosing the ability to probe faster processes [18, 24, 37]. To probe faster molecular processes, proper complementary fluorescence techniques are required. This aspect will be discussed in this thesis.

All FRAP experiments in this thesis were performed on a Leica SP5 scanning confocal microscope. HeLa cells and embryos expressing EYFP-Ran and Bcd-EGFP, respectively, were imaged using the 488 nm line of an Argon ion laser, with the power highly attenuated in order to eliminate visible photobleaching during recovery imaging. Both 100% and 50% laser intensity powers were used on the other hand for permanently photobleaching a selected region of interest, where the mobility of the protein is investigated. A glycerin–immersion objective lens (Leica 63x) was used in conjunction with a 320 μm pinhole.

1.4.4 Fluorescence Correlation Spectroscopy (FCS)

Fluorescence correlation spectroscopy (FCS) is a powerful tool used to study different dynamical aspects of molecular processes [23, 31, 38, 39]. When molecules of interest are fluorescently tagged, any molecular process that causes temporal fluctuations of the detected fluorescence intensity can be dynamically characterized using FCS. Examples of such processes include the diffusive motion of molecules in and out of a laser-beam focal volume, molecular complex formation, transient binding, structural conformational changes and photophysical

properties of fluorophores. The introduction of the confocal microscope concept, the advancements made in the fabrication of aberration-free optical components, the improvements in detector's sensitivity, the introduction of the green fluorescent protein and its variants for fluorescent labeling of proteins and the possibility of fast data acquisition and processing are all contributors to the technical advances that have revolutionized the use of FCS in the past decade, and have allowed its application to the study of living systems [22, 40].

The principle of FCS is the statistical correlation analysis of the spontaneous fluorescence fluctuations collected from a small detection volume, usually the subdiffraction limited detection volume of a confocal microscope. In the confocal geometry, the excitation volume is defined as the laser beam focal volume, and the volume from which fluorescence is collected is further reduced by the introduction of a pinhole in the back focal plane of the objective. The resulting detection volume can be mathematically approximated as a three-dimensional Gaussian volume. Since the detection volume has no physical boundaries, and can be manipulated in time and space, FCS is a non-invasive technique allowing for real-time dynamical measurements in live biological systems [38, 40].

One of the main factors causing fluorescence fluctuations in a FCS experiment is the diffusion of fluorophores across the detection volume, caused by the thermal energy fluctuations of the medium surrounding the fluorescent particle. The characteristic duration of a fluctuation caused by fluorophore diffusion corresponds to the average residence time of the particle in the detection volume. In order to obtain reliable information about the dynamical behavior of a type of particle, a statistical analysis on a large number of individual fluctuations is required. This is achieved by computing the correlation function of the signal, $G(\tau)$. Analysis of this function assuming that the cause of the fluctuations is known and can be modeled gives information about the dynamical processes underlying the fluctuations. In the case of diffusion, the diffusion coefficient of the particles and their absolute concentration can be retrieved. If several different fluorophores are present, their different diffusion coefficients and the relative amplitude of their contribution to the correlation function can also in principle be obtained [40].

The home-built system used for the presented FCS experiments in this thesis has been described in detail elsewhere [11]. Briefly, a water-immersion objective lens (Nikon 60x, NA=1.2) was used to focus the laser beam and to collect the fluorescence signal. Before each series of experiments, a dye with predetermined diffusion coefficient (at room temperature) was used. From this calibration, both w_0 and z_0, the $1/e^2$ radii of the 3D Gaussian detection volume in the directions perpendicular and parallel to the optical axis, respectively, were determined. All experiments were carried out at very low laser intensities (I ~ 2 μW, corresponding to a ~0.5 kW/cm^2 flux at the sample) for photobleaching effect elimination or at least minimization.

Individual autocorrelation functions were analyzed using three different models. First a model accounting for the possibility of multiple diffusing components and protein blinking was used:

$$G(t) = \frac{1}{N}\left(1 + \frac{B}{1-B}e^{-t/\tau_B}\right)\sum_{i=1}^{n}\frac{A_i}{\left(1 + \left(t/\tau_{D,i}\right)\right)\sqrt{1 + \left(t/\tau_{D,i}\right)/S^2}} + C. \qquad (1.4.4.1)$$

The characteristic time $\tau_{D,i}$ is related to the diffusion coefficient of the ith species, D_i, and to the half-width of the detection volume, w_0: $\tau_{D,i} = w_0^2/4D_i$. A_i is the amplitude of the term related to the ith species. N is the average number of fluorescent proteins in the detection volume. For n=1, A_1=1. For n=2, and in the case when both fluorescent species have the same molecular brightness, A_1 and A_2 are the respective fractions of species 1 and 2. S is the aspect ratio of the detection volume ($S=z_0/w_0$), which was fixed in our analysis to a pre-determined value obtained during a calibration step. The exponential term is related to the protein alternating between a fluorescent and a non-fluorescent state: B is the fraction of proteins found in the dark state and τ_B is the relaxation time associated with the blinking. The constant term C was added to account for very slow processes such as global cellular/embryonic motions that result in the autocorrelation function relaxing to a slightly non-zero value at large times.

The Pearson correlation coefficient, r, was calculated to test the hypothesis of the lack of correlation between $\tau_{D,1}$ and $\tau_{D,2}$ for pairs of data points when considering a 2-component diffusion model (Eq. (1.4.4.1), n=2):

$$r = \frac{n\sum \tau_{D1}\tau_{D2} - \sum \tau_{D1}\sum \tau_{D2}}{\sqrt{\left(n\sum \tau_{D1}^{2} - \left(\sum \tau_{D1}\right)^{2}\right)\left(n\sum \tau_{D2}^{2} - \left(\sum \tau_{D2}\right)^{2}\right)}};$$
(1.4.4.2)

where n is the number of pairs of data points being correlated, and in this work it represents the number of FCS measurements taken in a specific compartment, nucleus or cytoplasm.

Second, a model taking into account the possibility of anomalous diffusion was used in some cases for comparison. As mentioned earlier in this introduction, several factors modify the behavior of freely diffusing particles in biological systems. Crowding, sieving effects, protein complex formation and transient binding of proteins to other cellular structures alter protein mobility from simple diffusion to anomalous diffusion. To test for the existence of such effects, anomalous diffusion model was used. Although unable to isolate the different factors that cause such behavior or their amplitudes, anomalous diffusion model fitting is one of the steps that could be used to identify the existence of such effects. Knowledge of the system under investigation as well as the employment of other models is required to isolate the different contributing factors to this subdiffusive behavior. The following formula is used to fit the FCS data with anomalous diffusion model [11]:

$$G(t) = \frac{1}{N}\left(1 + \frac{B}{1-B}e^{-t/\tau_{B}}\right)\frac{1}{\left(1 + (t/\tau_{D})^{\alpha}\right)\sqrt{1 + (t/\tau_{D})^{\alpha}/S^{2}}} + C;$$
(1.4.4.3)

where α is the anomalous diffusion exponent and it measures the extent of deviation from a purely diffusive behavior. For obstructed diffusion, the value of the exponent $\alpha < 1$. As seen in Eq. (1.4.4.2), the model was adjusted to account for fluorescence blinking of EYFP and EGFP. Two-component diffusion model and anomalous diffusion model are often used to describe diffusion in cells [41].

We also used a stick-and-diffuse model to analyze the average autocorrelation function obtained for nuclear FCS data. The premise of that model is that fluorescent molecules interact with one type of immobile ligands according to a simple exponential kinetics, where the molecules bind to their ligand with a rate k_{on} and unbind with a rate k_{off}. The distribution of binding times is exponential with an average value $1/k_{off}$. Molecules are freely diffusing between

two binding events, with a diffusion coefficient D. An expression for the autocorrelation function expected in the case of 2D diffusion has been recently derived by Yeung et al. [13]. We adapted that expression for 3D diffusion, and added a blinking contribution:

$$G(t) = \frac{1}{N}\left(1 + \frac{B}{1-B}e^{-t/\tau_B}\right)\left[\frac{e^{-k_{off}t}}{1+k_{off}/k_{on}} + \frac{1}{1+k_{on}/k_{off}}\frac{e^{-k_{on}t}}{\left(1+t/\tau_D\right)\sqrt{1+t/\left(S^2\tau_D\right)}} + \frac{k_{on}k_{off}}{k_{on}+k_{off}}\right.$$

$$\left.\sum_{n=1}^{\infty}\frac{1}{(n-1)!\,n!}\int_0^t ds\frac{e^{-k_{off}(t-s)-k_{on}s}}{\left(1+s/\tau_D\right)\sqrt{1+s/\left(S^2\tau_D\right)}}\left(2n+k_{off}s+k_{on}(t-s)\right)\left(k_{on}k_{off}s(t-s)\right)^{n-1}\right] + C. \quad (1.4.4.4)$$

Least-square fitting of Eq. (1.4.4.1) and Eq. (1.4.4.4) to the data was performed using the software Kaleidagraph and the software Maple, respectively. The Maple code used for FCS data analysis with the stick-and-diffuse model is included in Appendix A.

1.4.5 Raster-Image Correlation Spectroscopy (RICS)

RICS is an extension of the principle of FCS to the analysis of time-series of confocal laser scanning images. When such images are collected under carefully selected scanning conditions, it allows studying the dynamics of the system under investigation over a much larger time range, in particular it allows studying processes slower than those accessible by FCS [32, 34]. A spatio-temporal correlation function, $G_S(\xi,\psi)$, is first calculated from pixel-to-pixel and line-to-line correlations in each image. Because the different pixels in a laser-scanning confocal image have been in fact recorded at different times, this correlation function results from both spatial and temporal correlations. Stack of images are used for better correlation averaging.

The following equation, assuming simple diffusion of a single species, is then used to fit the spatio-temporal autocorrelation function [34]:

$$G_S(\xi,\psi) = \frac{1}{N}\left(1 + \frac{4D\left(\tau_p\xi + \tau_l\psi\right)}{w_0^2}\right)^{-1}\left(1 + \frac{4D\left(\tau_p\xi + \tau_l\psi\right)}{w_z^2}\right)^{-1/2}\exp\left(-\frac{\delta r^2}{w_0^2}\left(\xi^2 + \psi^2\right)\bigg/\left(1 + \frac{4D\left(\tau_p\xi + \tau_l\psi\right)}{w_0^2}\right)\right); \quad (1.4.5.1)$$

where ξ and ψ are the spatial increments along the fast and slow axis of the raster image, respectively. δr is the pixel size, τ_p is the pixel dwell time and τ_l is the time between lines. w_0 and

w_z are the radial and axial waists of the detection volume, respectively. The fit returns a value for the diffusion coefficient of the fluorescent particle, D, and the average number of molecules found in the confocal volume, N.

Our data was collected using the laser scanning confocal microscope as for N&B analysis (Nikon EZ C1, v.3.2) but with different set of scanning conditions, and analyzed using the SimFCS software. We consistently used the moving average feature of the software, meaning that an average image was calculated every 4 images and subtracted from each individual image before the computation of the autocorrelation function. This feature ensures that spatial correlations due to cellular features do not appear in the calculated autocorrelation function. The reader will find detailed description of scanning conditions used to collect image stacks for this analysis in the relevant sections of this manuscript.

Part 2   Spatial Distribution and Mobility of the Ran GTPase in Live Interphase Cells

Abstract

The small GTPase Ran is a key regulator of nuclear pore complex mediated nucleo-cytoplasmic transport. To examine how Ran distribution and mobility contributes to its role in nuclear transport, we analyzed the behavior of an EYFP-Ran fusion protein in HeLa cells using several quantitative fluorescence imaging techniques. Similar to the endogenous Ran, on average ~70% EYFP-Ran localized to the nucleus. In contrast to previous reports, we observed no immobile fractions of EYFP-Ran in cells. The majority of the EYFP-Ran molecules were freely diffusing but a smaller population of EYFP-Ran displayed significantly slower mobility, resulting in an overall average apparent diffusion coefficient of ~5 μm^2/s. The fraction of slower moving EYFP-Ran was larger within nuclei, suggesting that nuclear ligands such as RCC1 or transport receptor complexes strongly influence the nuclear dynamics of Ran. The average residence time of Ran at the nuclear envelope was measured to be ~20 ms and we estimate that at steady state ~200 endogenous Ran molecules are present at each nuclear pore complex. This high number suggests that in addition to being present at the nuclear pore within transport complexes, Ran might also dynamically associate with the nuclear envelope, thereby raising the effective concentration of the protein around the pores.

2.1 Background

The GTPase Ran is a highly conserved member of the Ras superfamily of GTP-binding proteins (see Figure 1). It is involved in many functions supporting the compartmentalization of the eukaryotic cell genome in interphase and in its segregation to daughter cells by the mitotic spindle during cell division. The guanine nucleotide exchange factor for Ran, RCC1, is a DNA- and histone-binding protein localized in the nucleus [42, 43]. In contrast, the only identified RanGTPase activating protein, RanGAP, is a cytoplasmic protein localized in vertebrate cells is enriched at the cytoplasmic side of the nuclear pore complex (NPC) through its association with the nucleoporin RanBP2/Nup358 [44]. As a result of this organization, nuclei in interphase vertebrate cells contain high concentrations of Ran in its GTP-bound form, while in the cytoplasm, Ran exists mostly in its GDP-bound form [45]. As RCC1 also dynamically interacts with chromosomes in cells undergoing open mitosis, the position of the genome in eukaryotes is always marked by a high local concentration of RanGTP, the so-called RanGTP gradient [46].

Figure 1. X-Ray Diffraction Structure of RanGTP at 2.7 Å resolution [47]. Adapted from the Protein Data Bank.

Ran regulates nuclear transport via its interaction with nuclear transport receptors of the importin β/karyopherin superfamily [48]. The binding of RanGTP to nuclear import receptors (importins) that are in complex with their nuclear localization signal (NLS) containing cargoes induces cargo dissociation. As a consequence, importin-RanGTP complexes return to the cytoplasm, while NLS cargoes accumulate in the nucleus. The export of nuclear export signal

containing cargoes is mediated by their complexes with nuclear export receptors (exportins) that become stable only in the presence of RanGTP [45] (see Figure 2). As a result, every nuclear import or export event results in the depletion of at least one Ran molecule from the nucleus. The nuclear pool of Ran is replenished by active nuclear import of RanGDP to nuclei by its dedicated nuclear importer NTF2, a small dimeric protein [49].
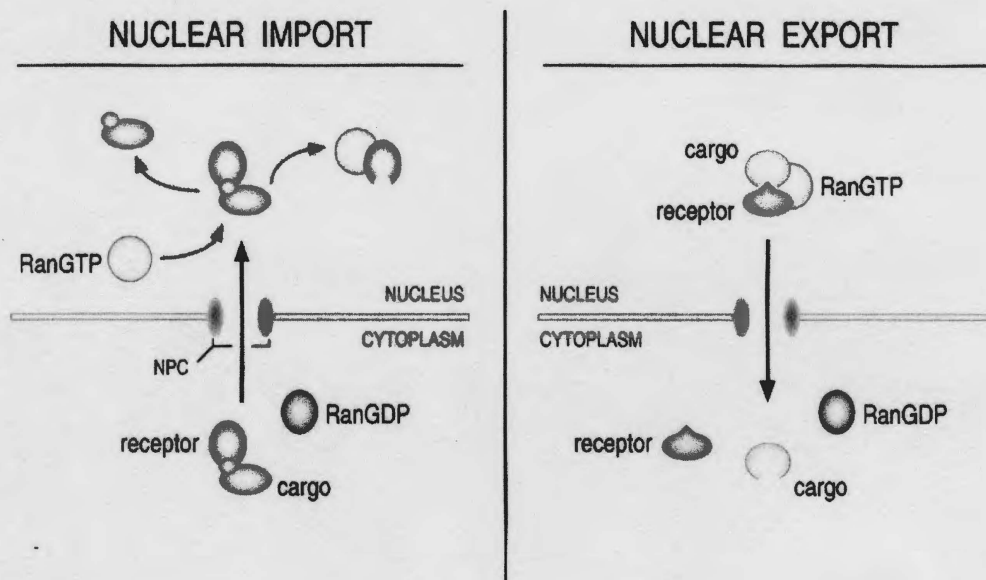
Figure 2. Nuclear import and export cycles. As illustrated here, Ran is a major regulator of both cycles through its role in unloading the imported cargo and uploading the exported cargo in the nucleus [50].

The expected steep RanGTP gradient driving the nuclear transport [51, 52] is paralleled by a Ran protein concentration gradient across the nuclear envelope (NE) [51, 53-57]. A significant Ran concentration gradient surrounding condensed chromosomes is also evident in cells undergoing open mitosis [55]. The origin of the Ran protein concentration gradient has not been clarified. Some studies have underlined the importance of NTF2, which facilitates the passage of cytoplasmic RanGDP through the NPCs [49, 51]. In addition, Ran is known to have numerous binding partners in the nucleus [58-60], including the chromatin-bound proteins RCC1 [54, 61], histone H3 and histone H4 [62]. Associations with large or stationary proteins could

explain how the Ran protein concentration gradient is maintained even during mitosis in the absence of a NE [55, 63] (retention mechanism).

Mobility is an important aspect of the cellular behavior of Ran, in particular its mobility around the chromosomes which one would expect to be significantly reduced if the retention mechanism hypothesis were true, and its mobility at the NE where disassembly of the cargo-nuclear transport receptor complexes presumably takes place [64]. Only recently, measurements of Ran cellular mobility have been attempted as part of a large study aiming at quantifying the mobility of nuclear transport receptors [57]. In that study, recombinant Ran, which was fluorescently labeled with an organic dye, was introduced in cells by microinjection, and its mobility was characterized by fluorescence correlation spectroscopy (FCS) and continuous photobleaching. Several distinct Ran populations were observed, including an immobile fraction, and a fraction of molecules diffusing as fast as in aqueous solution, an observation difficult to reconcile with the high viscosity of the cytoplasm.

In the present study, we revisited the question of Ran's cellular mobility using an EYFP-Ran fusion protein in order to avoid possible artifacts due to the presence of free dye, and using several complementary fluorescence techniques to corroborate our findings. As is detailed below, our results indicate that Ran is mobile throughout the cell, with no significant immobile fraction, but with a considerably reduced mobility in the nucleus as compared to the cytoplasm. This reduced mobility concurs with the active role played by nuclear RanGTP, but it is not large enough for us to conclude that retention mechanisms play a significant role, at least in interphase. We also observed relatively long residence time of EYFP-Ran at the NE (~20 ms), consistent with the idea that the population of Ran present at NPCs is composed of Ran both transported through NPC channels and engaged in the formation or dissociation of transport cargoes.

2.2 Materials and Methods

2.2.1 Cell culture and transfection

HeLa cells were obtained from ATCC, The Global Bioresource Center. Cells were maintained at 37°C, 5% CO_2 and 95% humidity, in α–MEM medium supplemented with 10% FBS and 100 μg/ml Normacine. The pEYFP-C1 plasmid (Clontech) was used to prepare HeLa cell lines stably expressing EYFP. For expression of EYFP-Ran, the EYFP sequence (Clontech) was cloned to the N-terminus of Ran, and then inserted in a pSG8 backbone. HeLa cells were transfected using ExGen500 according to the protocol suggested by the manufacturer (Fermentas). In the case of EYFP, transfected cells were selected by using 0.4 mg/mL neomycin to obtain stably expressing cell lines. For imaging, HeLa cells were plated on 18x18 mm glass coverslips for 24 hours, then washed in phosphate-buffered saline (PBS, pH=7.4) at 37°C, and immediately mounted on a 24x40 mm microscope slide with the help of parafilm spacers. Cells were kept in PBS during experiments. For FCS experiments the cells were kept at 37°C with the help of both a heated stage and an objective heater (Linkam Scientific). Each live cell sample was used for a maximum of 2 hours before being discarded. For the detection of endogenous Ran by immunofluorescence, fixed HeLa cells were incubated with mouse monoclonal anti-human Ran antibody (IgG2a, BD Transduction laboratories; Franklin Lakes, New Jersey) diluted 1:3000 for 2 hours, washed and incubated with anti-mouse goat IgG labeled with Alexa-488 (1:200; Molecular probe; Eugene, Oregon) for 1 hour. The cells shown in Fig. 3E&F were fixed using paraformaldehyde (2%) in PBS at 37°C for 30 minutes. The immunofluorescence labeling and imaging was done by Josh Ng-Kamstra towards his 4th year undergraduate project.

2.2.2 Live cell confocal imaging for fluorescence intensity analysis, N&B analysis and RICS

The setup used to collect confocal fluorescence intensity images is described in part1 (section 1.4.1) (Nikon EZ C1, v.1.7). Imaging conditions were optimized to minimize fluorescence photobleaching while maximizing the signal-to-noise ratio. Namely, images were collected with a 10 or 15 μs dwell time, and with a pixel size varying between 80 nm and 310

nm. Also, the detector gain was adjusted for each cell depending on the level of expression of the fluorescent protein, to ensure a large dynamic range in the image while keeping the maximum level of signal collected well below the detector saturation level. To quantify the level of fluorescence intensity in different cellular compartments we used the software ImageJ, as described in later sections. For RICS and N&B analysis, images were collected with the same laser scanning microscope as for fluorescence quantification (Nikon EZ C1, v.3.2) but using slightly different scanning conditions. Because RICS analysis relies on calculating the fluorescence autocorrelation between adjacent pixels in the same row and those in consecutive rows, so scanning speeds (dwell times) are chosen so that they match the mobility of the fluorescent molecules under investigation. Scanning speeds were varied constantly in an effort to characterize the optimal dwell times that matches molecular dynamics in cells. Being instrumentally limited by a minimal dwell time of 5 μs, a dwell time range of 8–29 μs was selected in this case (EYFP-Ran and EYFP in cells). When selecting a pixel size (that is the distance between two consecutive pixels), a "good" pixel size is one that gives a high detection volume overlap between two consecutive pixels, in order to capture sufficient number of independent spatial samples. That increases the number of independent spatial fluorescence fluctuations collected and improves our chances of detecting the spatial decay of a molecule undergoing dynamical process while scanning the surroundings [34]. Given the size of the detection volume in the commercial microscope used for imaging (w_0=0.3–0.4 μm), pixel sizes in the range 30-120 nm were explored. A pixel size of 60 nm was selected in the end, based on the good quality of the correlation signal. This pixel size was then kept constant throughout RICS and N&B experiments. Generally, stacks of 256x256 pixel images, with 80 images per stack, were collected for averaging of the correlation function calculated. Images were collected at room temperature and at a laser power of ~5 μW at the sample.

2.2.3 Fluorescence intensity analysis

The level of fluorescence intensity in different cellular compartments was quantified using the software ImageJ. The fluorescence associated with different cellular regions was assessed from images by selecting several rectangular areas in each of those regions and by

taking the average fluorescence intensity in each area. The overall average fluorescence intensity in each compartment was then calculated to represent a single fluorescence intensity measurement in the selected compartment. The average fluorescence intensity of different compartments was then compared for different cells. This allowed extracting relative concentration ratio as will be emphasized in the results section. The fluorescence at the nuclear envelope on the other hand was measured by using very thin rectangular areas extending on either side of the NE. The row of pixels with the highest fluorescence intensity corresponded to the NE, and was compared to the average fluorescence in the nucleus. The fluorescence intensity values obtained were normalized to the detector's gain and the pixel dwell time. To calculate the NE concentration of Ran, c_{NE}, relative to its nuclear concentration, c_N, we took into account the fact that the NE is thin compared to the confocal volume waist, with the height of the NPCs only ~0.08 μm [4] whereas the diameter of the confocal volume was $2w_0$~0.7 μm. Thus signals coming from the nucleus and cytoplasm also contribute to the fluorescence reading at the NE. Taking into account the ellipsoidal geometry of the confocal volume, we estimate that:

$$c_{NE} \cong c_N \omega_0 \left(\frac{I_{NE}}{I_N} - \frac{1}{2}\left(1 + \frac{I_C}{I_N}\right) \right) ; \tag{2.2.3.1}$$

where I_{NE}/I_N is the NE-to-nuclear fluorescence intensity ration and I_C/I_N is the cytoplasmic-to-nuclear fluorescence intensity ratio. This calculation assumes similar molecular brightness of EYFP throughout the cell, which was proven to be valid using N&B analysis.

2.2.4 Fluorescence Recovery after Photobleaching (FRAP)

FRAP experiments were performed on a Leica SP5 confocal microscope. Cells were imaged using the 488 nm line of an Argon ion laser, with the power highly attenuated in order to eliminate visible photobleaching during imaging. A selected circular region of the cell with diameter d~2.5 μm was photobleached using 50% of the laser's full power for 2 frames (1.3 s/frame). Finally, a small square region (15.7 μm²) encompassing the photobleached area was imaged to detect fluorescence recovery in and out of the photobleached region of interest. Pre-bleach, bleach, and post-bleach imaging (of 256x256 pixel images) was carried out at a 700

lines/s scanning speed and with a 15.5 nm pixel size. Different combinations of scanning speeds, pixel size, bleached area size and laser excitation powers were explored in an attempt to determine the best scanning conditions with minimal fluorescence photobleaching effects on the pre-bleach and post-bleach image collection. The above chosen scanning conditions yielded minimal photobleaching effects and high signal-to-noise ratio in fluorescence recovery traces.

2.2.5 Fluorescence Correlation Spectroscopy (FCS)

A home-built FCS system was used for the presented FCS experiments (see section 1.4.4). A water-immersion objective lens (Nikon 60x, NA=1.2) was used to focus the 514 nm line of an Argon ion laser and to collect the fluorescence signal. Before each series of experiment, Rhodamine 6G (Sigma) was used to determine the size of the detection volume, assuming a room temperature diffusion coefficient for Rhodamine 6G $D=250\mu m^2/s$. From calibration with Rhodamine 6G, it was found that $w_0=0.3$–0.4 μm, depending on the optical alignment. Experiments were carried out at very low laser intensities of $I \sim 2$ μW in which case no reduction in overall fluorescence intensity was observed over the time of a measurement (60-120 s), indicating negligible photobleaching effects. Cells with very low expression rates resulted in a low signal-to-noise ratio. On the other hand, very bright cells saturated the detector. My choice of cells was those with moderate expression rates yet a high signal-to-noise ratio. In all the cells studied the concentration of fluorescent protein was calculated to be less than 100 nM. Similar choice of cell expression rate was applied for cells selected for FRAP experiment. All measurements were collected in interphase cells with a very clear nucleoli and nuclear membrane.

Individual autocorrelation functions were analyzed using the 2-component diffusion model to account for two visible dynamical processes (Eq. (1.4.4.1), n=2). The Pearson correlation coefficient, r, was calculated to test the hypothesis of the lack of correlation between $\tau_{D,1}$ and $\tau_{D,2}$ for pairs of FCS data points analyzed using the 2-component diffusion model.

Both EYFP and EYFP-Ran exhibited a clear and consistent fluorescence blinking in the autocorrelation data recorded in HeLa cells. This blinking process was accounted for in the data

analysis (see Eq. (1.4.4.1)). The constant term C always represented less than 5% of the total amplitude of the average nuclear and cytoplasmic correlation function. Seven independent parameters were varied during the fit (A_1/N, A_2/N, $\tau_{D,1}$, $\tau_{D,2}$, B, τ_B, C).

The stick-and-diffuse model was used to analyze the average autocorrelation function obtained for nuclear Ran to test for the possibility of transient binding processes (Eq. (1.4.4.4)). A blinking term was also added in this case to account for the above mentioned blinking process. Least-square fitting of Eq. (1.4.4.4) to the data was performed using the software Maple. As for the two-component diffusion model, seven independent parameters are varied during the fit (N, D, B, τ_B, k_{on}, k_{off}, C).

2.2.6 Raster-Image Correlation Spectroscopy (RICS)

Live cell scanning confocal images with optimized imaging conditions (as mentioned in section 2.2.2) were analyzed using SimFCS. The moving average feature of the software was consistently used, meaning that an average image was calculated every 4 images and subtracted from each individual image before the computation of the autocorrelation function. This is necessary for removal of spatial correlations due to cellular features and cell motion corrections. Eq. (1.4.5.1) was used to fit the spatial autocorrelation data after skipping the zero spatial-lag data point of the ACF decay to avoid possible instrumental correlated shot noise.

2.2.7 Line-scanning FCS

Line scan analysis was performed on confocal data obtained by repeatedly scanning the same line in the sample. Each line was imaged 30720 times. A two-dimensional intensity matrix representing fluorescence intensity as a function of pixel position and time was built, and the temporal ACF at each pixel of the line was computed using the software SimFCS. ACFs were fitted using a 1-component simple diffusion model (Eq. (1.4.4.1), n=1 and B=0). We chose to scan along 1 to 4 μm lines, using 256 pixels, a pixel size of 4–16 nm to ensure that several pixels would be on the NE, and a pixel time of 3.6 μs, resulting in a line time of 695 μs.

2.3 Results

2.3.1 Spatial distribution of EYFP-Ran in live interphase cells

Confocal images of HeLa cells transiently expressing EYFP-Ran showed a steep concentration gradient across the NE, with EYFP-Ran residing preferably in the nucleus (Fig. 3A). From the image intensity analysis of numerous interphase cells we found the nuclear-to-cytoplasmic fluorescence ratio to be 3.9±0.4 for EYFP-Ran, and 1.01±0.04 for the control protein EYFP (Fig. 3C). In addition, a marked accumulation at the NE was observed for EYFP-Ran, but not for EYFP. In live cells expressing EYFP-Ran, we found that the NE-to-nucleus fluorescence intensity ratio, where the NE fluorescence is calculated as the highest fluorescence intensity recorded along a line crossing the NE, was 1.28±0.07 (Fig. 3D). Finally, the fluorescence intensity of both EYFP and EYFP-Ran was slightly lower in nucleoli compared to the rest of the nucleus. The nucleolar-to-nuclear fluorescence ratio was found to be 0.66±0.02 for EYFP-Ran and 0.52±0.01 for EYFP (Fig. 4), an indication that Ran is actively imported or retained in nucleoli.

In order to discuss the cellular distribution of EYFP-Ran and its similarity to that of endogenous Ran, a representative image showing the distribution of wild-type endogenous Ran, as observed by immunofluorescence with monoclonal Ran antibody are shown in Fig. 3E. The cell has been fixed, immunolabeled and imaged by a 4th year thesis student in the lab, Josh Ng-Kamstra. The typical fluorescence distribution observed in these cells differed from that observed in live cells transfected with EYFP-Ran in two ways. First the nuclear-to-cytoplasmic ratio was lower (3.1±0.5) and second there was no visible accumulation of the protein at the nuclear envelope. To understand whether these differences were due to an actual difference in the localization of the two proteins, we evaluated the effect of cell fixation by imaging fixed cells that had been transfected with EYFP-Ran (Fig. 3F). We found that in fixed cells the nuclear-to-cytoplasmic ratio of EYFP-Ran also decreased (to 3.5±0.2) and that at the same time, the prominent localization of the protein at the NE disappeared. This indicates that the fixation process perturbs the observed cellular distribution of Ran, and that fixed cells cannot be used to quantify this distribution (more details are found in the discussion section of this part).

Fluorescence intensity detected by the fluorescence microscope is the product of the concentration and the specific molecular brightness of the fluorophore. So, intensity is not necessarily a direct indication of protein concentration since molecular brightness might depend on cellular localization. In order to obtain a direct comparison of the concentration of EYFP-Ran in different cellular compartments without the potential bias of differential molecular brightness, we used particle number and brightness analysis (N&B) analysis (see materials and methods). A representative example is shown in Fig. 5, where the average intensity image of a HeLa cell expressing EYFP-Ran was separated into a map of the average number of EYFP-Ran molecules per pixel and map of their molecular brightness. The N&B analysis demonstrated that the molecular brightness of EYFP-Ran is similar throughout the cells, corroborating the intensity-based analysis. It also confirmed that EYFP-Ran is non-uniformly distributed across the cell, accumulating in the nucleus and at the NE.

When the pixels with background signal from outside of cells were disregarded, the N&B analysis showed that pixels from the cytoplasm contained on average the lowest number of EYFP-Ran molecules, and that as expected pixels from nuclei formed a distinct population with significantly higher EYFP-Ran molecule numbers (Fig. 5B). The ratio of the average number of the EYFP-Ran molecules in nuclear vs. cytoplasmic pixels was ~4, similar to fluorescence intensity quantification. Pixels from nucleoli contained intermediate EYFP-Ran molecule numbers compared to nucleus and cytoplasm. Also consistent with the fluorescence intensity measurements, the highest numbers of EYFP-Ran molecules per pixel in individual cells were detected in small spot-like clusters along the NE. As a control, N&B analysis was also performed for cells transfected with EYFP (Fig. 6). As for EYFP-Ran, the molecular brightness map inside the cell was very uniform. However, because the concentration of EYFP is relatively uniform in HeLa cells, the nuclear and cytoplasmic pixel populations could not be distinguished on the corresponding correlation plot.
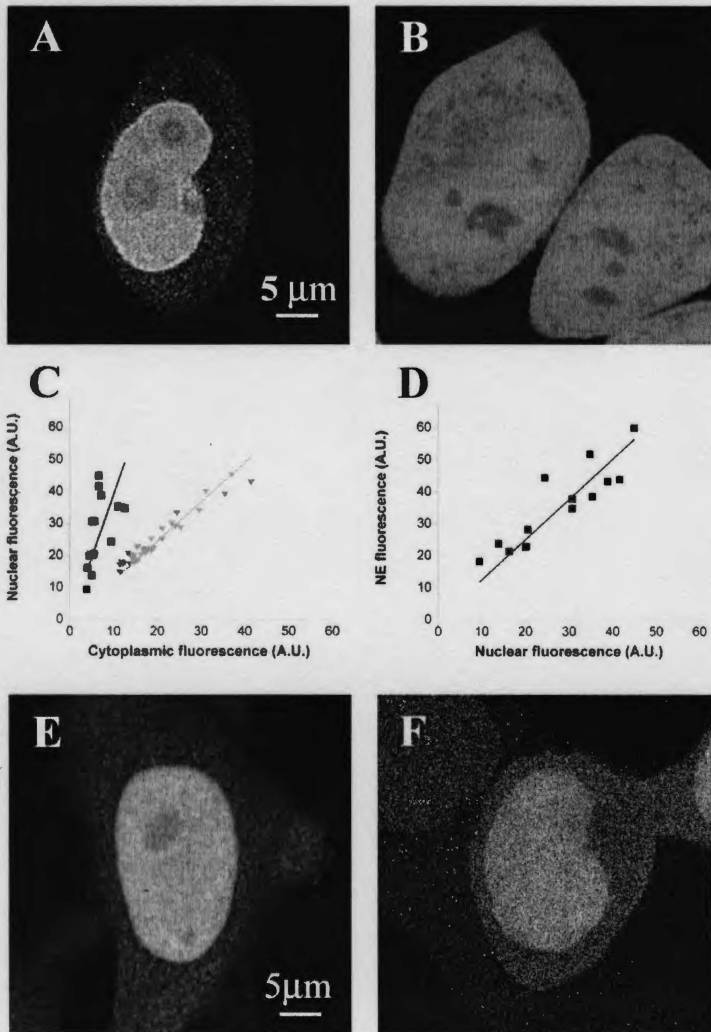
Figure 3: Cellular distribution of EYFP-Ran in interphase cells: Fluorescence intensity analysis. (A) Typical fluorescence confocal image of a HeLa cell expressing EYFP-Ran. (B) Typical fluorescence confocal image of HeLa cells expressing EYFP. (C) Nuclear-to-cytoplasmic fluorescence intensity for EYFP-Ran (black squares) or EYFP (gray triangles). Each point represents different cell. (D) NE-to-nuclear fluorescence intensity for EYFP-Ran. (E) Fluorescence intensity confocal image of a fixed HeLa cell treated with an antibody against wild type Ran. Image courtesy of Josh Ng-Kamstra. (F) Typical fluorescence confocal image of a HeLa cell expressing EYFP-Ran after fixation. Scale is 5 μm in all images.
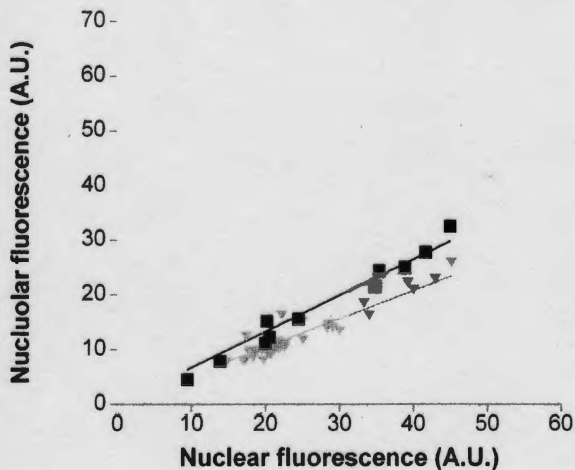
Figure 4: Nucleolar-to-nuclear fluorescence intensity of EYFP-Ran. The nucleolar-to-nuclear fluorescence intensity ratio of EYFP-Ran (black squares) is slightly larger than that of the control protein EYFP (gray inverted triangles).
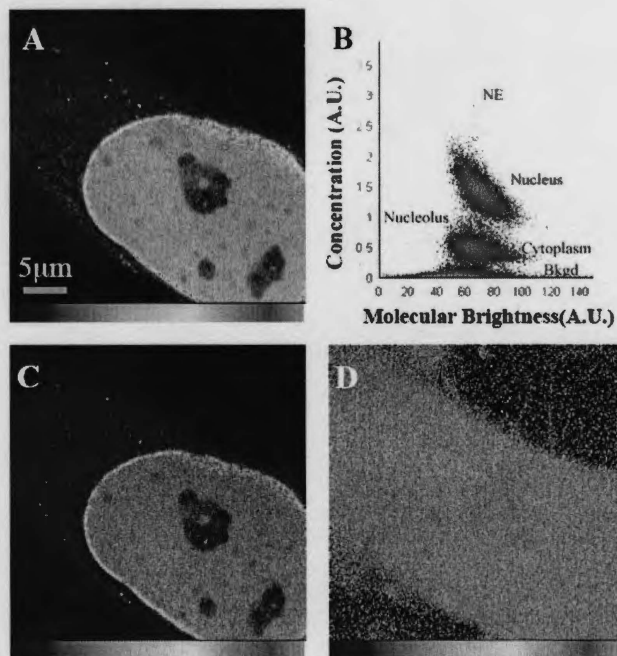
Figure 5: Cellular distribution of EYFP-Ran as seen with N&B analysis. (A) Average intensity map of an interphase HeLa cell expressing EYFP-Ran. (B) Correlation between the average concentration, <N>, and the average molecular brightness, B, of the fluorophore at each pixel of the image shown in A. The plot shows four distinct pixel populations. (C) Concentration map and (D) Molecular brightness map associated with (A).
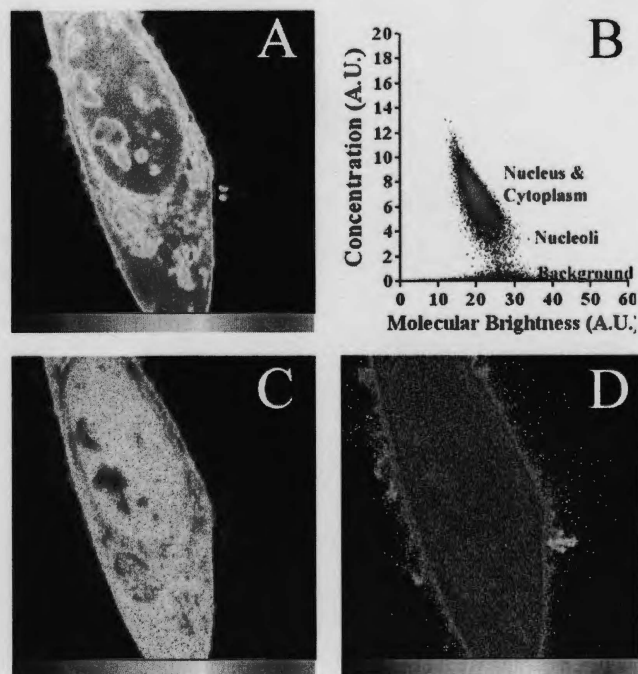
Figure 6: Cellular distribution of EYFP as seen with N&B analysis. (A) Average intensity map of an interphase HeLa cell expressing EYFP. (B) Correlation between the average concentration, <N>, and the average molecular brightness, B, of EYFP at each pixel of the image shown in A. (C) Concentration map retrieved from A. (D) Molecular brightness map retrieved from A. Image size is 24.1x24.1 μm.

2.3.2   Mobility of cytoplasmic and nuclear Ran using FRAP

We applied fluorescence recovery after photobleaching (FRAP) as a method well suited to detect potential slow or immobile populations of EYFP-Ran in cells. Selected small nuclear or cytoplasmic regions of cells transfected with EYFP-Ran were photobleached, after which a slightly larger region including the photobleached area was repeatedly imaged to capture the recovery process. The fluorescence in the photobleached area was normalized to the final average fluorescence outside of the photobleached area to account for fluorescence loss due to the continuous imaging (Fig. 7). Both in the nucleus and in the cytoplasm we consistently observed a 100% recovery with a half-time for recovery $\tau_{1/2}=0.9\pm0.4$ s in the nucleus and $\tau_{1/2}=0.7\pm0.7$ s in the cytoplasm. This demonstrated that all EYFP-Ran molecules in both compartments were therefore completely mobile on the ~1s time-scale, under our experimental conditions.
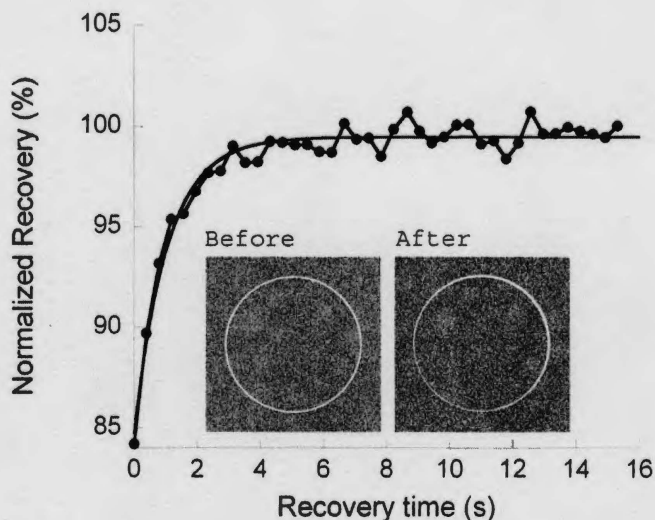
Figure 7: Fluorescence recovery after photobleaching in the nucleus of HeLa cells expressing EYFP-Ran. The plot shows the fluorescence recovery inside the photobleached area, normalized to the fluorescence measured immediately outside of this area. The line corresponds to a single-exponential fit and returned a recovery time of $\tau_{1/2}$~1 s. Inset: Confocal images of the scanned area before fluorescence photobleaching and at t=16 s after photobleaching, showing a complete fluorescence recovery. The circle indicates the photobleached area (diameter d=2.5 μm).

2.3.3   Comparison of Ran mobility in nucleus and cytoplasm using FCS

To refine our understanding of the dynamic behavior of EYFP-Ran, we performed single-point fluorescence correlation spectroscopy (FCS) measurements. Under low excitation intensity conditions producing no detectable bleaching during the course of the measurement, we performed 174 separated FCS measurements in multiple locations in the nucleus and the cytoplasm of 6 different HeLa cells expressing EYFP-Ran and compared them with 106 measurements in 9 HeLa cells expressing EYFP. The average autocorrelation functions obtained from these experiments are shown in Fig. 8. The autocorrelation functions obtained for EYFP were mainly consistent with free diffusion, as shown by the fact that they could be fitted very well (both in the cytoplasm and nucleus) using a 1-component diffusion model (Eq. (1.4.4.1), n=1). On the other hand, the autocorrelation functions obtained for EYFP-Ran contained a visible contribution from slower dynamical processes on top of free diffusion, as shown by the fact that using a 2-component diffusion model (Eq. (1.4.4.1), n=2) dramatically improved the fit to that data (Fig. 8 & χ^2 in Table 1). Note that the oscillations visible in the residuals above ~10 ms are due to mechanical vibrations caused by the laser fan, which could not be entirely suppressed. Despite these oscillations, it is clear that passing from a 1-component to a 2-component model does not improve the fit of the EYFP correlation data, but that it does improve the fit of the Ran-EYFP correlation data. To understand the molecular behavior underlying these differences, we analyzed the data in two different ways.

First, we used the 2-component diffusion model to analyze each individual correlation function recorded, retrieving two diffusion coefficients for each individual measurement (Fig. 9). These two diffusion coefficients were not correlated according to the Pearson's correlation coefficient calculated r=0.03 (Eq. (1.4.4.2)), supporting the assumption that two independent molecular processes are responsible for these two observed dynamics. According to this analysis, the majority of the signal from EYFP throughout the cell (~96%) was contributed by rapidly diffusing molecules (with a diffusion coefficient D=23±5 μm^2/s in the cytoplasm and D=21±5 μm^2/s in the nucleus). Similarly, for cytoplasmic EYFP-Ran, ~90% of the autocorrelation data corresponded to fast diffusing molecules (with D=15±6 μm^2/s, only ~45% lower than for

cytoplasmic EYFP), while only ~10% displayed a much slower motion (D=0.7±0.4 $\mu m^2/s$). In sharp contrast, slowly moving nuclear EYFP-Ran molecules (D=1.3±0.5 $\mu m^2/s$) contributed 33% of the signal. The remainder 67% of the nuclear EYFP-Ran seemed to be diffusing freely, with a diffusion coefficient (D=17±6 $\mu m^2/s$) only ~20% smaller than that of nuclear EYFP. Based on this two-component FCS analysis, we estimate that the average diffusion rate of the entire EYFP-Ran population in the nucleus was approximately ~12 $\mu m^2/s$, compared to ~14 $\mu m^2/s$ in the cytoplasm.

The distribution of diffusion coefficients shown in Fig. 9 is very wide. To check whether these variations reflected actual variations in the protein mobility for different locations in each of these compartments, we performed repeated measurements in different locations of the same cellular compartment. We observed time after time that when a measurement was repeated in the exact same location, the values of the measured diffusion coefficients were consistent, whereas when the location of the measurement was changed, a variation in the measured diffusion coefficients was often observed (Fig. 10). Thus, the variations observed from one location to another are indicative of a real dependence of the protein mobility on cellular location even within a single compartment.

Second, to consider the possibility that the slower fraction of EYFP-Ran was due to transient association of Ran with relatively immobile cellular structures in the cell nuclei, we also analyzed our nuclear data with the stick-and-diffuse model [13] using Eq. (1.4.4.4). The best statistically significant fit of the average autocorrelation function recorded in cell nuclei was found for D=17 $\mu m^2/s$, k_{on}=12 s^{-1} and k_{off}=31 s^{-1}, corresponding to 28% of the nuclear EYFP-Ran molecules being bound to nuclear structures at all times (Fig. 11). According to this analysis, each EYFP-Ran molecule is therefore immobilized 28% of the time, which means that its overall mobility corresponds to an average diffusion coefficient D=12 $\mu m^2/s$. Although the statistical significance of the stick-and-diffuse model was not as good as that of the two-component diffusion model (Table 1), both analyses converged on predicting that ~1/3 of nuclear EYFP-Ran is dynamically engaged in molecular interactions decreasing its mobility to D~12 $\mu m^2/s$.
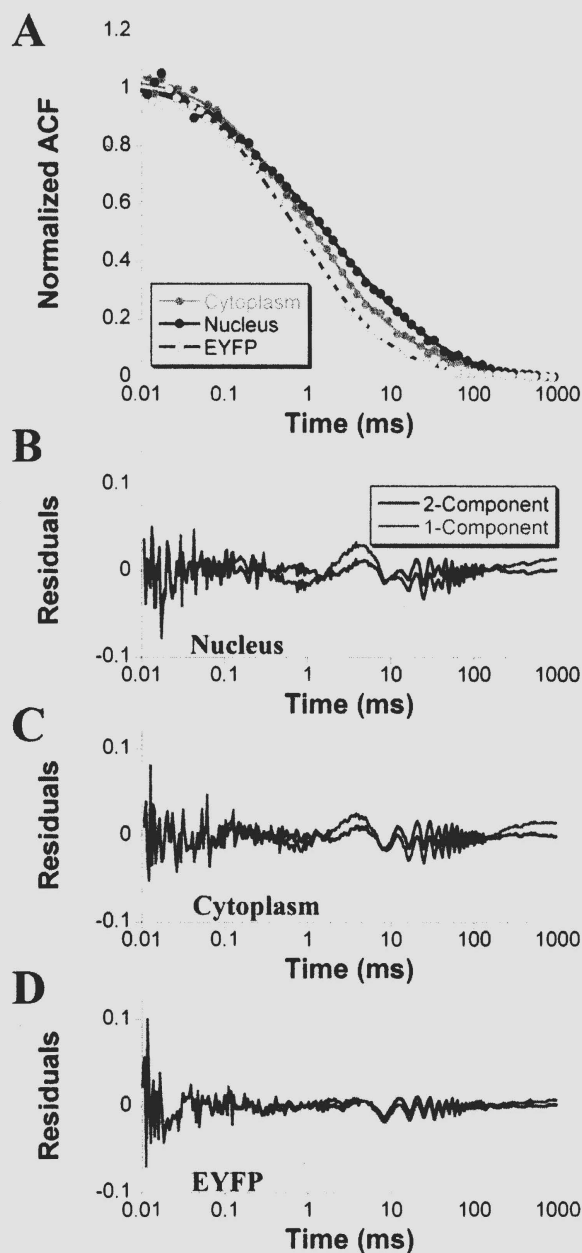
Figure 8: Analysis of the average autocorrelation functions with 1- and 2-component diffusion models. (A) Comparison between the average autocorrelation functions obtained for EYFP-Ran in the nucleus and cytoplasm of HeLa cells (filled black symbols and filled grey symbols, respectively) with the average autocorrelation function obtained for EYFP in the nucleus of HeLa cell (open circles). The lines correspond to 2-component diffusion model fit. The residuals for each of these three autocorrelation functions are shown in (B), (C) and (D) respectively, where the red lines correspond to the residuals obtained using a 1-component fit, and the black lines to those obtained using a 2-component fit.
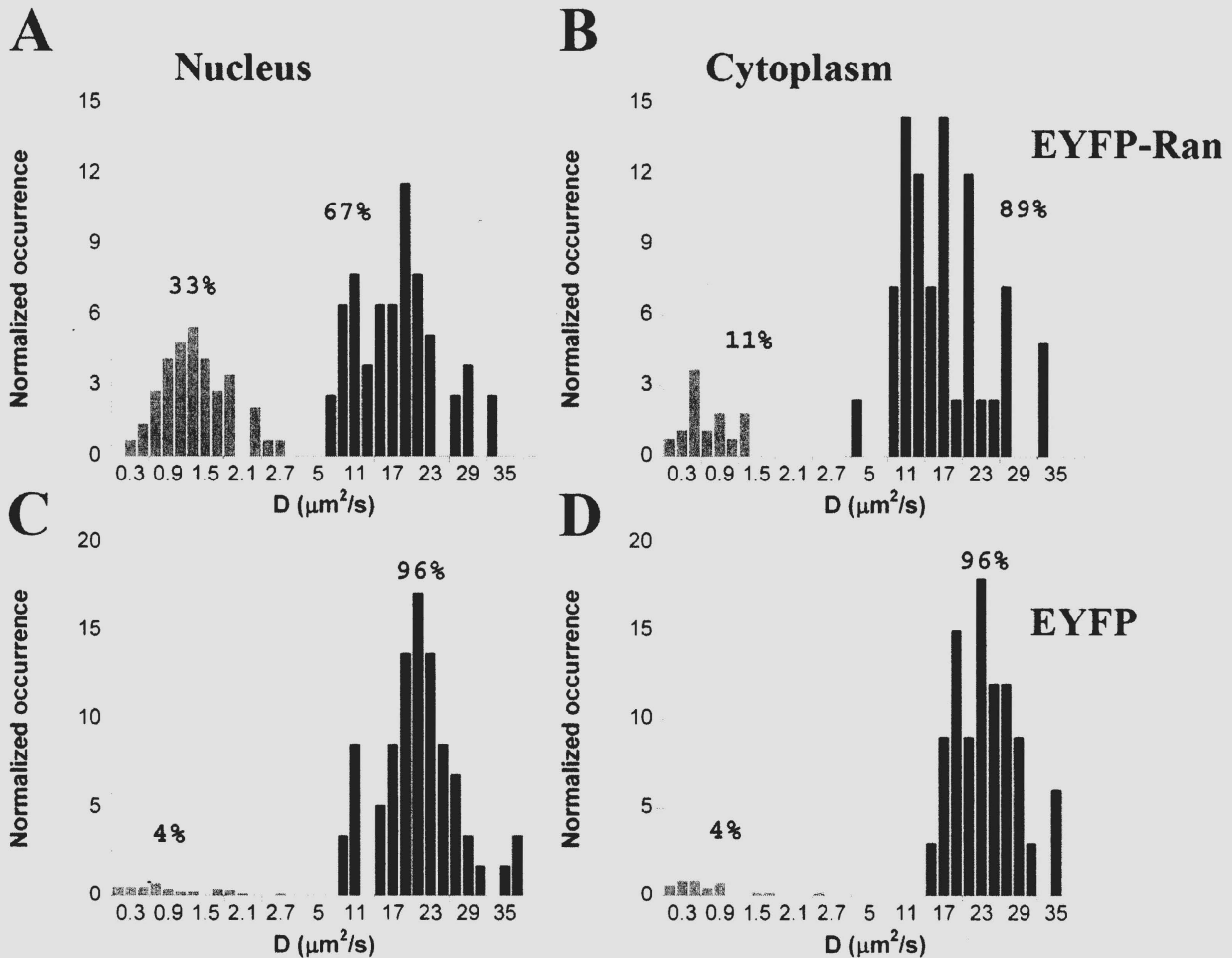
Figure 9: Distribution of diffusion coefficients obtained from analysis of the FCS data with the 2-component diffusion model for EYFP-Ran and EYFP. Black columns correspond to fast diffusion process and gray column to slow diffusion process. The total occurrence for each process has been normalized to its average relative weight in the correlation function. (A, B) Diffusion coefficients obtained for EYFP-Ran in the nucleus (A) and cytoplasm (B) of interphase HeLa cells. (C, D) Diffusion coefficients obtained for EYFP in the nucleus (C) and cytoplasm (D) of interphase HeLa cells. All data in this figure have been obtained for a laser power at the sample I=2 μW. Note that the scale for the diffusion coefficients (x-axis) is not linear.
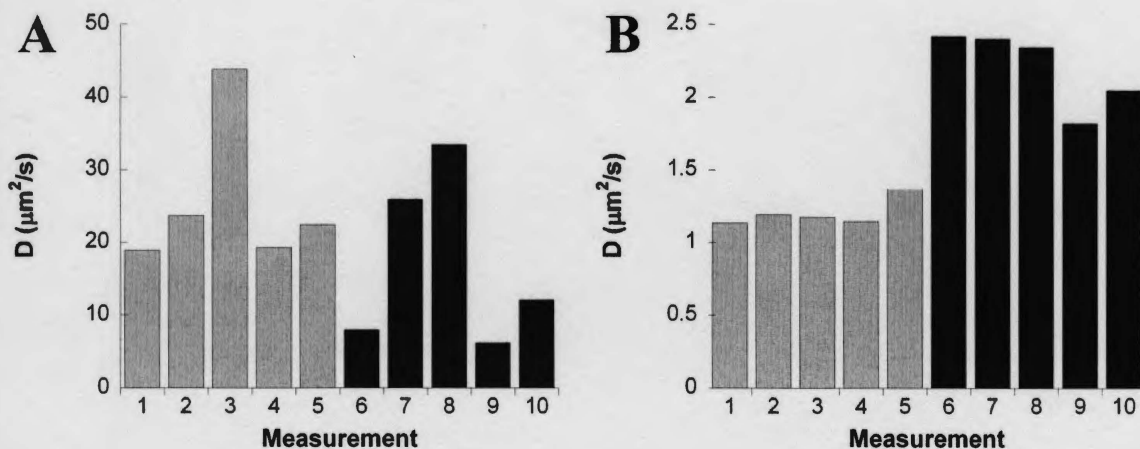
Figure 10: Reproducibility of FCS measurements in cells. Diffusion coefficients corresponding to the fast (A) and slow (B) components of the motion of EYFP-Ran for a series of consecutive measurements done in the nucleus of the same interphase HeLa cell. Grey bars correspond to measurements done in a first location, and black bars to measurements done in a second location.
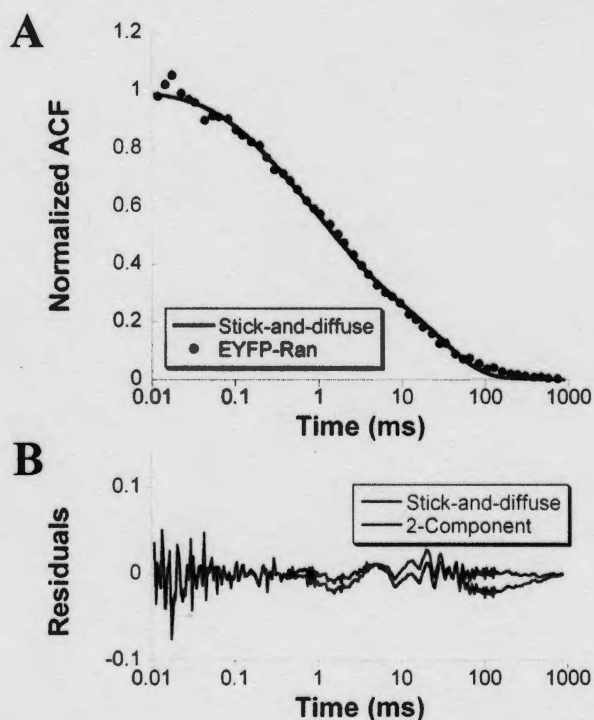
Figure 11: Analysis of the average autocorrelation function obtained for nuclear EYFP-Ran with the stick-and-diffuse model. (A) Nuclear EYFP-Ran data (filled black symbols, same as in Fig. 8A), fit to the result of the stick-and-diffuse model (blue line). The corresponding residuals are shown in **(B)** (blue line), and compared to those obtained using the two-component diffusion model (black line).

Model	$D_1(\mu m^2/s)$	$D_2(\mu m^2/s)$	$A_1(\%)$	$A_2(\%)$	$k_{on}\ (s^{-1})$	$k_{off}(s^{-1})$	χ^2
Nuclear EYFP-Ran 1-component diffusion	3.8	-	100	-	-	-	0.063
Nuclear EYFP-Ran 2-component diffusion	17	1.3	67	33	-	-	0.035
Nuclear EYFP-Ran Stick-and-diffuse	17	-	71	28	12	31	0.058
EYFP 1-component diffusion	14	-	100	-	-	-	0.043
EYFP 2-component diffusion	21	1.5	96	4	-	-	0.039

Table 1: Summary of the results obtained from the different models used to fit the nuclear EYFP-Ran and EYFP FCS data. The parameters for the 1- and 2-component diffusion models are defined in Eq. (1.4.4.1). Those for the stick-and-diffuse model are defined in Eq. (1.4.4.4). χ^2 is the chi square value with the weight for all data points set to 1. EYFP-Ran results are compared to that of EYFP FCS results, fit to 1- and 2-component diffusion model.

2.3.4 Fluorescence blinking of EYFP

Both EYFP and EYFP-Ran exhibited a clear and consistent fluorescence blinking in the autocorrelation data recorded in HeLa cells. A term accounting for this blinking of the EYFP chromophore was included in the autocorrelation analysis as explained above. Two parameters were recovered from this analysis, the blinking relaxation time and the ratio of non-fluorescent over fluorescent molecules. The distributions of these parameters as obtained in the nucleus of EYFP-Ran transfected HeLa cells are shown in Fig. 12. The blinking relaxation time was found to be 0.3±0.1 ms and the blinking ratio to be 0.3±0.1 (the errors have been estimated by fitting the distribution to a Gaussian function).
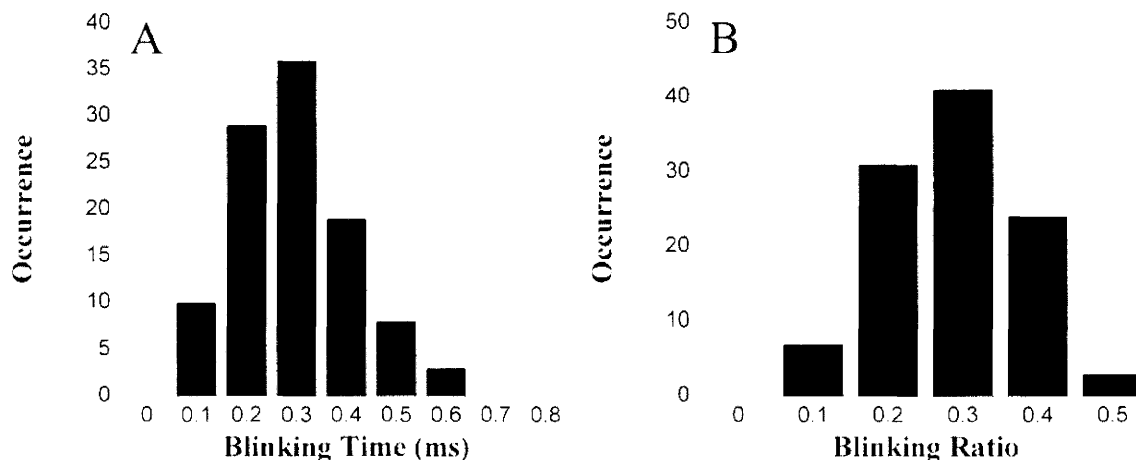
Figure 12: Distribution of blinking relaxation times (A) and ratios (B) obtained for EYFP-Ran in the nucleus of interphase HeLa cells.

2.3.6 Average apparent diffusion coefficient of nuclear Ran using RICS

Although FCS is a useful method to determine the concentration, diffusion coefficient and molecular interactions of mobile fluorescent molecules in living cells, immobile fluorescent molecules may remain invisible to FCS due to photobleaching [65, 66]. On the other hand, our measurements of Ran mobility with FRAP would not detect fast diffusing EYFP-Ran due to the relatively long time (2.6 s) needed to photobleach the chosen area. In an attempt to circumvent the limitations of both FCS and FRAP and measure the average diffusion coefficient of the entire EYFP-Ran population we used raster-image correlation spectroscopy (RICS) [32]. In RICS, the analysis of the spatio-temporal pixel-to-pixel and line-to-line correlations in raster-scanned images is used to extract information on very wide range of diffusion rates. Under scanning conditions optimized to achieve minimal photobleaching, we recorded time-series of confocal images of HeLa cells expressing EYFP or EYFP-Ran and calculated the corresponding spatio-temporal autocorrelation functions (Fig. 13) (Eq. (1.4.5.1)). As the amount of signal needed to obtain statistically significant autocorrelation functions was limiting in our conditions, the EYFP-Ran scans were analyzed over a rectangular region covering the entire nucleus and a small adjacent portion of the cytoplasm. Several pixel dwell times were investigated to verify the stability of this analysis. The average apparent diffusion coefficient of EYFP detected by RICS

was 18±2 μm^2/s, indistinguishable from FCS measurements. Although RICS measurements of the cytoplasmic EYFP-Ran could not be obtained due to limited signal, the average mobility of the mostly nuclear EYFP-Ran detected by RICS was 5.3±0.3 μm^2/s, i.e. significantly slower than EYFP alone and in the lower range of the estimated average diffusion coefficient of EYFP-Ran detected by FCS (~12 to 14 μm^2/s, with an error of ~6 μm^2/s).
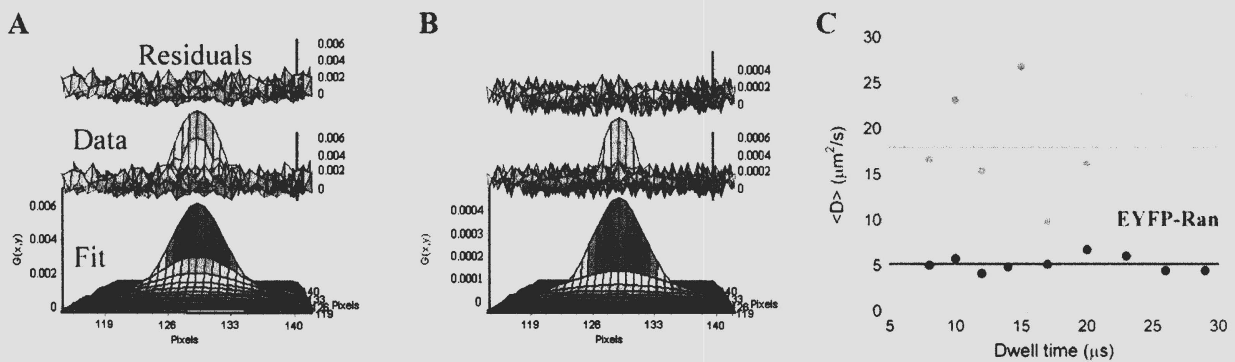
Figure 13: Ran dynamics as observed by RICS. (A) Example of an autocorrelation function obtained by RICS for a cell expressing EYFP-Ran (middle plot, dwell time of 10 μs and a pixel size of 0.06 μm). The corresponding fit (lower plot) and residuals (upper plot) are also shown. The diffusion coefficient recovered from this particular data was D=5.4 μm^2/s. (B) Example of an autocorrelation function obtained by RICS for a cell expressing EYFP (middle plot, obtained for a dwell time of 8 μs and a pixel size of 0.06 μm). The corresponding fit (lower plot) and residuals (upper plot) are also shown. The diffusion coefficient recovered from this particular data was D=17 μm^2/s. (C) Average diffusion coefficient obtained by RICS for EYFP-Ran and EYFP in interphase HeLa cells as a function of dwell time (black and gray symbols). The solid lines indicate the average value over all dwell times, <D>=5 μm^2/s for EYFP-Ran and <D>=18 μm^2/s for EYFP.

2.3.7   Residence time of Ran at the nuclear envelope

In principle, FCS could be used to analyze the dynamics of EYFP-Ran molecules associating with NPC directly. However, the conventional spot FCS measurements at NPCs are frustrated by the contribution of cytoplasmic and nuclear fluorescence background due to the relatively large size of the diffraction-limited confocal excitation volume compared to NPCs. Such measurements therefore require relatively high excitation intensities in order to pick up the signal coming from the NPCs, which can easily result in photobleaching. In order to measure the

mobility of EYFP-Ran at the NPC in comparison with the surrounding compartments, we performed linear confocal scanning combined with FCS analysis over several μm lines spanning the NE in HeLa cells expressing EYFP-Ran. Compared to single-point FCS, the line-scanning FCS reduced the average light flux on each individual pixel and therefore photobleaching, at the cost of a loss in temporal resolution. A temporal autocorrelation was calculated for individual pixels or groups of pixels along the lines using SimFCS (Fig. 14). No temporal correlation was observed in groups of pixels that were exclusively nuclear or cytoplasmic. On the contrary, clear temporal correlation in NE pixels was observed in groups of pixels crossing the NE. Analysis of the autocorrelation functions calculated at the NE, using a simple diffusion model (Eq. (1.4.4.1), n=1, B=0), returned an average residence time of 17±8 ms (obtained from 9 separate measurements).
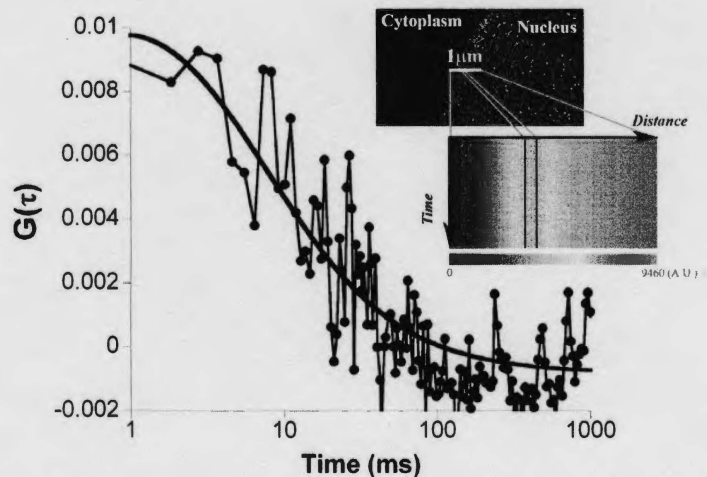
Figure 14: Line scan analysis. Autocorrelation function obtained from a line scan performed across the NE of a cell expressing EYFP-Ran, for pixels at the NE (black symbols). Fit of the data with a simple one-component diffusion model (Eq. (1.4.4.1) with n=1 and B=0) returned a residence time τ_D=10 ms in this case. Inset: Position of the line-scan with respect to the NE of the EYFP-Ran transfected HeLa cell (top) and intensity carpet corresponding to the line scan (bottom).

2.4 Discussion

2.4.1 Nuclear versus cytoplasmic localization

The preferential nuclear localization of Ran is widely documented, but has not often been carefully quantified. Two types of techniques had been so far applied to monitor Ran localization in vertebrate cells: detection of endogenous Ran by antibodies in fixed cells and detection of fluorescently labeled exogenous Ran by live cell imaging. Our fluorescence intensity measurements showed that EYFP-Ran concentration in nuclei was on average 3.9 times larger than that in the cytoplasm. Importantly, this result was corroborated by N&B analysis showing that the EYFP-Ran molecular fluorescence brightness was constant throughout the cell. The high nuclear accumulation of EYFP-Ran that we detected was slightly higher than nuclear-to-cytoplasmic intensity ratio in microinjected dye-labeled Ran imaged in live HeLa cells (~1.9-3.5 depending on labeled Ran concentration, thus our data corresponds well with the data reported at low labeled Ran concentration) [51]. It is also higher than nuclear-to-cytoplasmic ratio detected for endogenous Ran by immunofluorescence in fixed HeLa cells, which we found to be 3.1±0.5, and was previously reported to be 2.4 by Kelley and Paschal [56]. However, the decrease in nuclear-to-cytoplasmic ratio and disappearance of the NE localization of EYFP-Ran we observed for cells expressing EYFP-Ran after fixation (using different fixation protocols) suggests that commonly used fixation methods do not prevent dislocation of most NE-bound and potentially the leakage of a fraction of nuclear Ran to the cytoplasm.

Another way to compare our data on the nuclear localization of EYFP-Ran to that obtained on the nuclear localization of endogenous Ran is to consider the relative total quantity (as opposed to concentration) of Ran present in nucleus and cytoplasm, as this can be measured using immunoprecipitation methods, and therefore requiring neither fluorescence labeling or fixation [51, 53]. Assuming that the nuclear-to-cytoplasmic volume ratios is 2:3 in HeLa cells [52] we estimated that on average 72% of the EYFP-Ran molecules were present in HeLa cell nuclei. On the other hand, previous studies have found that wtRan is 80 to 90% nuclear in BHK21 cells [51, 53]. The nuclear vs. cytoplasmic localization of EYFP-Ran we detected is thus consistent with measurements of the localization of endogenous wild-type Ran for which cells

have not been fixed. In the future, live imaging of endogenous fluorescently labeled Ran, for example using RNAi-assisted gene replacement and small molecule tag [67], could be used to validate our results obtained with transiently expressed EYFP-Ran.

Nuclear-to-nucleolar fluorescence intensity ratio shows that both proteins, EYFP and EYFP-Ran, tend to be excluded from the nucleoli. However, this tendency is not as marked for EYFP-Ran. This means that the fusion protein, although it is larger than the control protein EYFP, has better access to the nucleolar area of the nucleus, and suggests that Ran may be recruited to nucleoli.

2.4.2 Cellular mobility of Ran

We did not detect any immobile fraction for EYFP-Ran, in agreement with the previous observation that the fluorescence due to nuclear dye-labeled Ran can be completely depleted by photobleaching cytoplasmic fluorescent Ran in the same cell [51]. On the other hand, based on the photobleaching losses observed during continuous confocal spot excitation of dye-labeled Ran injected to cells, Paradise et al. had reported immobile fraction of fluorescent Ran in nuclei (33±13 %) and cytoplasm (29±28 %) [57]. However, it is likely that the decrease in fluorescence they observed was in fact due to the bleaching of mobile Ran molecules, since fluorescence excitation of a limited pool of fluorophores present within a single cell is known to result in overall decrease of fluorescence even for mobile particles [68]. Because of the time scale of our FRAP experiments and our non-selective choice of measurement sites in the cytoplasm and in nuclei, it should be noted that our experiments do not exclude the possibility that small populations of Ran are locally immobilized on rare cellular structures. A small fraction of Ran was for example detected in association with centrosomes [69], but it is not know how stable this localization is.

Our RICS and single point FCS analyses gave a coherent picture of the mobility of EYFP-Ran as compared to that of EYFP. A virtually identical high diffusion coefficient of the control protein EYFP was detected by RICS and FCS (~20 μm^2/s) indicating that EYFP is freely diffusing in cells, as anticipated. A similar diffusion coefficient for EGFP expressed in HeLa

cells (23 ± 5 $\mu m^2/s$) was detected by FCS [51] and for EGFP expressed in CHO-K1 cells (21 ± 5 $\mu m^2/s$) by RICS [32].

According to our FCS measurement, the majority of EYFP-Ran throughout the cells displayed mobility with a diffusion coefficient 15 to 17 $\mu m^2/s$. If Ran behaved in cells as an inert molecule similar to EYFP, the diffusion coefficient of free EYFP-Ran (52 kDa) would be ~20% -50% slower than that of EYFP (25 kDa), depending on the geometry of the fusion protein. The observed large fractions of rapidly diffusing EYFP-Ran molecules therefore likely correspond to EYFP-Ran in either unbound form or present in small complexes.

Interestingly, our FCS measurements also showed the presence of a second population of EYFP-Ran molecules displaying a reduced mobility. In the cytoplasm this population was quite small (~10%), consistent with the lack of known stable cytoplasmic ligands for the presumably mostly GDP- bound cytoplasmic Ran. In the nucleus on the other hand, the slow moving fraction represented a significant ~30% of the Ran population. In the analysis of our RICS data, a characteristic signature of the slower mobile population of EYFP-Ran was the presence of line-to-line correlations (visible in Fig. 13A for EYFP-Ran, but not for EYFP in Fig.13B).

Both the two-component and stick-and-diffuse models we applied to analyze our FCS data concurred that at any time ~30% nuclear EYFP-Ran was involved in molecular interactions. The difference between the average diffusion rate of the nuclear vs. cytoplasmic pool of EYFP Ran (~12 $\mu m^2/s$ vs. ~14 $\mu m^2/s$) is too small to explain the accumulation of Ran in the nucleus on its own, highlighting the importance of Ran's active nuclear import.

The unbinding rate of EYFP-Ran extracted using the stick–and–diffuse model (k_{off} = 31 s^{-1}) was intriguingly comparable to the dissociation rate of the Ran-RCC1 complex (55 s^{-1}) [70]. However, the nuclear RCC1 concentration is estimated to be only ~0.4 μM [70] and can therefore account for only a fraction of the EYFP-Ran nuclear interactions detected by FCS. Because the majority of Ran nuclear interactions likely represent RanGTP binding to multiple NTRs that are presumably very stable in the absence of RanGAP and RanBP1 the two-component diffusion model likely better represents the behavior of the nuclear Ran population. The variation of diffusion coefficient obtained throughout the nucleus could be due to an uneven distribution of binding partner for Ran.

Although both fluorescence techniques, FCS and RICS, demonstrated that the average nuclear dynamical behavior of EYFP-Ran is much slower than that of EYFP, RICS results were skewed towards the slower motions of Ran resulting in a lower average diffusion coefficient than that captured using FCS. It was also noticed that RICS results are dependent on the number of data points skipped at the short spatial-lag before fitting the data to the spatial autocorrelation function in Eq. (1.4.5.1). The number of data points skipped depends on the confocal microscope shot noise that correlates at the zero spatial-lag. No correlated shot noise was detected when using non-fluorescent sample, and so skipping one data point was my choice since I was not given the option to skip zero points. In principle, skipping two points should not alter the average diffusion coefficient retrieved dramatically. For testing purposes, skipping two points resulted in significantly increasing the average diffusion coefficients for both EYFP and EYFP-Ran at all dwell times. The dependence of RICS results on the number of data points skipped is a reflection of the limitations of this technique, which could be related to the limited confocal scanning speeds available to us (dwell time ≥ 3.6 μs). Faster scanning speeds allow for collecting higher number of independent fluorescence fluctuations of the particle in motion (higher spatial sampling) increasing by that the robustness of the spatial autocorrelation function close to the short spatial-lags.

2.4.3 Accumulation of Ran at the nuclear envelope

Our observation of the EYFP-tagged wtRan accumulating at the NE agrees with previous live imaging studies performed with microinjected dye-labeled wtRan [51, 55, 57]. Given an estimated nuclear concentration $C_N \sim 6$ μM of endogenous wtRan in HeLa cells [51, 52, 54], and the 1.3 average NE-to-nuclear fluorescence intensity ratio measured by image fluorescence intensity analysis, we estimated that endogenous Ran must exist at the NE at an average surface concentration $C_{NE} \sim 800$ molecules of Ran/μm^2 NE. However, EYFP-Ran was not distributed evenly at the NE and the majority of its signal concentrated in small clusters that likely corresponded to individual NPCs (Fig. 3A and 5A). The majority of EYFP-Ran at the NE therefore appears to be present at NPCs where the N&B analysis indicated 3–3.5 higher EYFP-Ran concentration compared to the nucleoplasm. Taking into account the estimated ~4 NPC/μm^2

surface density of NPC at the NE [71] we calculated that about 200 endogenous wtRan molecules are concentrated around each NPC in HeLa cells. This is one order of magnitude larger than a previous estimate obtained in B104 neuroblastoma cells [57].

A part of the Ran visualized at the NE must correspond to RanGTP-NTR complexes exported to the cytoplasm and RanGDP-NTF2 complexes imported to the nucleus. On the other hand, if each of the 200 Ran molecules we observed were present at an NPC was being transported and considering the average residence time we measured for EYFP-Ran at NPCs (~17 ms), the corresponding flux through a single NPC would be ~10^4 Ran molecules s^{-1}. This exceeds the estimated maximal transport capacity of the NPC channel, 10^3 s^{-1}, by about 10 times [72].

In addition, the EYFP-Ran residence time we measured was longer than the average transit times through NPCs previously measured for other proteins using single-particle tracking in permeabilized cells: ~6 ms for NTF2, ~7 ms for transportin 1, and from 1 to 10 ms for a fluorescent NLS fusion protein depending on importin β concentration [71, 73, 74]. This comparison suggests that Ran spends more time around NPCs than the transport cargos it regulates, which also indicates that a significant fraction of the Ran observed at NPCs is not participating in the transition through NPC channels. It is possible that Ran accumulating at the nuclear face of NPCs facilitate termination of nuclear import reactions, e.g. through Nup50/Npap60-assisted dissociation of importin β cargos [75]. On the cytoplasmic NPC face, Ran could accumulate due to RanGTP and RanGTP-NTR complex binding to Ran-binding domains of RanBP2, a 358 kD nucleoporin forming cytoplasmic NPC fibers, prior to GTP hydrolysis on Ran catalyzed by RanGAP bound to RanBP2 via its SUMO tag [76, 77].

2.5 Conclusions

Using an EYFP-Ran protein fusion, we found that Ran displayed a significantly reduced mobility in the nucleus, consistent with the presence of a large number of binding partners available to RanGTP in that compartment. We estimated that about a third of nuclear Ran was engaged in molecular interactions at any time. This would result in an effective diffusion coefficient of $D \sim 10 \mu m^2/s$, which is not low enough to explain how Ran could be retained around the chromosomes in the absence of active nuclear transport, as Ran is small enough to freely diffuse out of the nucleus through the NPCs. However, it remains possible that the interaction of Ran with the chromatin is very different during mitosis. We observed a very significant accumulation of the protein at the nuclear membrane, and estimated that ~200 wtRan proteins are found in the vicinity of each NPC in HeLa cells. This accumulation must be at least in part due to frequent translocation of the protein through the NPCs, since each nuclear transport cycle is associated with the translocation of at least two Ran molecules, one imported and one exported. However since the number of wtRan per NPC is so high, and since the average dwell time of the Ran at the NE (~20 ms) is longer than the dwell times of nuclear transport receptors [71, 73, 74], this number exceeds the estimated transport capacity of the NPC suggesting that a significant fraction of Ran recruited to NPCs must not be directly translocating through NPC channels. Instead, the Ran residing at NPCs may correspond to RanGTP molecules accumulating at the nuclear side of NPCs, and engaging in the termination of nuclear import reactions or in the formation of nuclear export complexes. On the cytoplasmic side, there could also be accumulation of RanGTP-nuclear transport receptor complexes binding to Ran binding domains of RanBP2 prior to RanGAP-catalyzed GTP hydrolysis. To understand the mechanism of Ran-regulated nuclear transport, in the future it will be important to determine whether the above two scenarios indeed explain the observed Ran accumulation at NPCs or whether some other unknown function of Ran is involved.

Part 3   The Bcd Morphogenetic Concentration Gradient is Formed by Diffusion

Abstract

The morphogenic protein Bicoid is an essential activator of cellular differentiation and pattern formation in the fruit fly *Drosophila melanogaster*. This protein forms an exponential concentration gradient along the anterior-posterior axis of fly embryo and acts as a transcription factor that activates a cascade of target genes. How the gradient is established, however, remains controversial. The currently accepted model, known as the Synthesis, Diffusion & Degradation (SDD) model, assumes that the protein spreads across the embryo by simple diffusion, as was initially proposed by Francis Crick in 1970. This model, however, has been called into question by several recent studies. To test the hypothesis that the gradient is formed by diffusion, we studied the localization and dynamics of a Bcd-EGFP fusion protein in live embryos using complementary fluorescence techniques: Fluorescence Recovery after Photobleaching (FRAP) and Fluorescence Correlation Spectroscopy (FCS). We observed that Bcd-EGFP concentration decayed exponentially along the anterior-posterior axis of the embryo with a characteristic length of ~ 100 μm, as previously reported by other groups, and we estimated the absolute nuclear and cytoplasmic Bcd-EGFP concentrations at the anterior pole to be 120 nM & 15 nM, respectively. In the cytoplasm, we found that the overwhelming majority of Bcd molecules were undergoing diffusive motion, with an average diffusion coefficient D~5 $\mu m^2/s$. This is an important result, because it provides the first experimental evidence that the mobility of cytoplasmic Bcd is high enough to support the establishment of a concentration gradient across the embryo before the beginning of cellularization, as envisioned in the SDD model. We also observed that 35% of the nuclear Bcd population was engaged in transient binding to immobile structures, with an average binding time $\tau_B = 1/k_{off} = 120$ ms, a result consistent with the fact that Bcd functions as a transcription factor.

3.1 Background

The development of a multicellular organism from a single cell (the fertilized egg) is a fascinating phenomenon. In the fruit fly *Drosophila melanogaster*, the undifferentiated fertilized egg undergoes multiple nuclear divisions before cellular differentiation, where cells get assigned their fate in a future fully developed body according to their spatial location along the embryonic axes in the early stages of development. Cellular differentiation is the result of morphogenetic concentration gradients that diversify the genome products of cells in a concentration-dependent manner, giving rise to spatially and functionally different cells [78-82].

The story of embryonic cellular differentiation and pattern formation extends back to the beginning of the 20th century. It has been suggested then that gradients of "formative substances" could control pattern formation and provide axis polarity in developing embryos. These "substances" were thought to be metabolic molecules that form gradients in developing embryos when exposed to a stimulus [83, 84]. In 1969, Lewis Wolpert reinforced the concept of positional information where cells identify their position in the embryo depending on specific cellular parameters. He proposed that a concentration gradient of a chemical (morphogen) can provide a cellular parameter, where cells "learn" their position by "reading" the morphogen concentration. He proposed that cells respond differently to different concentration of the morphogen, and therefore different positions along the morphogen gradient give rise to different cell types (patterning) [81, 82]. Up until then, a morphogen was proposed to be a substance that forms a concentration gradient which induces multiple positive responses in embryonic cells in a concentration-dependent manner. Wolpert work inspired Francis Crick to mathematically prove that simple diffusion is a possible mechanism for setting up a steady linear morphogen concentration gradient over an embryo about 70 cells long in a reasonable time (3 hours) [80]. For his mathematical model, Crick postulated the existence of a morphogen source, where the morphogenetic molecules are synthesized at a constant rate at one end of the embryo, and a sink that destroys the morphogen at the opposite end, keeping it at a constant very low level. In between the source and the sink the morphogen was proposed to undergo diffusive motion with a constant effective diffusion coefficient. Crick's model was visionary and challenged the current

accepted knowledge, since at that time diffusion was not believed to occur in living tissues [85]. Indeed, all attempts to understand cellular differentiation and patterning through morphogen gradients were controversial at the time because of the lack of direct evidence for their existence.

The fruit fly *Drosophila melanogaster* represents an ideal system to understand cellular differentiation. The fully-sequenced well-studied easily-accessed genome of the fly, its short life span in comparison to other organisms (~14 days), its rapid reproduction (~400 embryos/fly), the fast embryonic development (~hours), as well as its unexpensive maintenance were all attractions to embryologists when selecting the *Drosophila melanogaster* as a model organism to investigate early pattern formation in embryos. A model organism is one which allows for analyzing a particular problem, such as embryonic development and cellular differentiation, hoping the answer retrieved can be generalized to other systems [86]. The female lays a 0.48 mm long fertilized egg contained in a chorion (shell). During fertilization, the mother deposits certain maternal genes that are vital for the development of the embryo. After fertilization, the embryo is a giant cell with a nucleus suspended in the cytoplasm. The nucleus undergoes multiple divisions without the formation of new cellular walls. Instead, nuclei remain suspended in the interior of the cytoplasm for the first eight divisions, after which they migrate to the cortical cytoplasm (at the periphery of the embryo) where the last five divisions before cellularization take place. During each of the corresponding five interphases, the nuclei form a two dimensional lattice below the membrane of the embryo. At the end of cycle 14, division pauses and cellularization begins, at which point the embryo builds cellular walls between nuclei forming cells with constant spatial separations of ~ 6 μm. The fully functional larva hatches within 24 hours of fertilization [79]. Cellular differentiation and patterning begins before cellularization, giving scientists a short but sufficient time window to study the secrets behind embryonic development.

In 1970, Christiane Nusslein-Volhard and Eric Wieschaus started the process of isolating a number of zygotic and maternal genes which when mutated disrupted pattern formation along the axes of *Drosophila melanogaster* embryos: the anterior-posterior axis, and the perpendicular dorsal-ventral axis [78]. While zygotic mutation effects were limited to small portions of the embryo [87-89], some maternal mutations dramatically affected the organization of the two perpendicular embryonic axes [79, 90-98]. Screening for mutation effects on embryonic

development rather than adult phenotype made possible monitoring the effects in undeveloped embryos (found not to hatch), which deepened our understanding of the dominant effects which could not be detected otherwise [99]. The *bicoid* gene (*bcd*) was identified in this context. Embryos from *bcd* mutant females were completely lacking anterior development. Soon after, the bicoid protein (Bcd) was identified as a key morphogen [9, 100] that forms a simple exponential concentration gradient along the anterior-posterior axis, with its highest amplitude at the anterior-most tip of the embryo, the source, and decaying to a near zero concentration at the posterior end [9, 100] (Fig. 15). The Bcd protein is the product of the strictly localized *bcd* mRNA at the anterior pole of the embryo [101, 102], which is maternally deposited in early oogenesis. This study provided us with the first molecular evidence for the existence of morphogen gradient since the proposal of the concept.
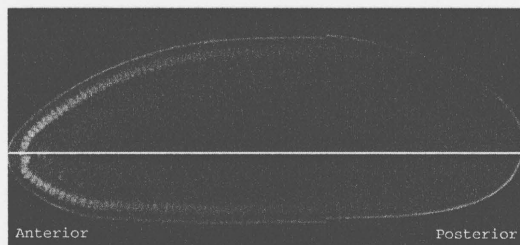
Figure 15. **Fluorescence intensity confocal image of a *Drosophila* embryo expressing Bcd-EGFP during nuclear cycle 14**. The anterior-posterior concentration profile is evidently exponential. Image courtesy of Aude Porcher.

One of the main functions of Bcd as a morphogen is its ability to promote the expression of zygotic genes along the axis of its distribution in early development in a concentration-dependent manner, simply by activating their translation. It was the presence of a homeobox domain, a common domain found in transcription factors, in the maternal *bcd* genes that hinted at the involvement of the Bcd protein in regulating the transcription of other genes by binding to their DNA sequence [101, 102] (see Fig. 16). This role is further supported by the predominant nuclear localization of the protein [100]. Different numbers of binding sites with different affinities for the Bcd protein were identified on the regulatory regions of zygotic *gap* genes [103-105]. Similarly, the products of the *gap* genes act as transcription factors themselves and regulate

the transcription of *pair rule* genes. When transcribed, the later ones activate *segment polarity* genes that are responsible for defining the larvae's segment numbers and boundaries [78, 79]. This hierarchy array of regulations, with the Bcd protein as its primary and key component, spatially defines the genome products of different cells along the anterior-posterior axis and so their eventual function in the whole organism.

Figure 16. The 3D NMR solution structure of the Bcd Homeodomain (purple, 15.9 kDa) bound to the DNA backbone [106]. Adapted from the Protein Data Bank.

The simplest and most widely accepted model proposed to explain the origins of the Bcd concentration gradient is referred to as the SDD model (SDD stands for Synthesis, Diffusion & Degradation). The model considers a local source where the morphogen is synthesized at a constant rate at one end of the embryo, with diffusion as the mechanism for morphogen translocation from the source across the embryo, and a spatially uniform degradation process of the first order keeping the overall concentration of the morphogen constant [80, 107-109]. This model is based on Crick's model, where diffusion and degradation are the mechanisms responsible for generating the morphogenetic concentration gradient [80], although the degradation mechanism chosen by Crick results in the prediction of a linear concentration gradient, instead of the observed exponential gradient. Instead, the simple exponential decay of Bcd concentration along the anterior-posterior axis is in agreement with the mathematical solution of the SDD model [109]. Yet, and in spite of a recent attempt to test its validity [108], it has not been experimentally demonstrated yet that the Bcd protein undergoes simple diffusion in the cytoplasm of *Drosophila* embryo, and nothing is known about the actual degradation process

for Bcd. The SDD model puts constraints on the value of the effective diffusion coefficient (D) of Bcd, because it predicts that D will influence two observable parameters: the decay length of the concentration gradient λ and the effective lifetime (τ) of Bcd, which also corresponds to the time necessary to establish the gradient. The former was measured to be ~ 100 μm [100, 110], and the latter was estimated to be 90 minutes at most [108]. According to the SDD model $\lambda^2/\tau=D$, therefore an effective diffusion coefficient of at least 2 $\mu m^2/s$ is necessary in order to form a concentration gradient corresponding to these experimental observations.

One way to test the different models proposed to explain the gradient establishment is to study Bcd protein dynamics throughout early *Drosophila* embryos. Two groups have made a documented attempt at getting an insight on the dynamics' behavior of Bcd [100, 108, 111]. One of these attempts was comparative rather than experimental [100]. Driever et al. relied on the results of previously published FRAP studies of injected macromolecules in the cytoplasm of mammalian cells [112] to validate their choice of the SDD model to explain the Bcd gradient formation. They estimated the effective diffusion constant of Bcd to be in the range of 0.3–1 $\mu m^2/s$ and they assumed Bcd was capable of generating a gradient over a 200 μm distance in about an hour {Driever, 1988a #65}. This comparison did not take into account the difference in viscosity and internal organization between mammalian cells and *Drosophila* embryos as well as the specific interaction Bcd might have with its environment. In a more recent study, Gregor et al. used a Bcd-EGFP fusion protein to test the stability of the Bcd gradient dynamics. They showed that the gradient was stably established in *Drosophila* embryos within 90 minutes of fertilization [108]. Their results indicated a rather remarkable reproducibility of the gradient among embryos, challenging in that earlier findings [110]. The authors also relied on a direct scanning confocal FRAP experiment for extracting dynamic constants of Bcd-EGFP in the cortical cytoplasm of *Drosophila* embryo during mitosis, in an attempt to test the validity of the SDD model [108]. Surprisingly however, the effective diffusion constant extracted was ~ 0.3–0.4 $\mu m^2/s$. According to the SDD model, this diffusion constant is too small to form the observed stable gradient by cycles 9–14. The authors proposed different alternatives to the origin of the Bcd gradient formation, and in so doing challenged the most widely considered and accepted model for morphogen gradient formation.

In the present study, we focus on studying the mobility of the fluorescently tagged Bcd-EGFP in the nucleus and cytoplasm of *Drosophila* embryos in stages 12–14, using two complementary fluorescence techniques to substantiate our findings: FRAP and the well-established single-point FCS. Our results indicate that Bcd is mobile throughout the embryo, with no detected immobility, with high diffusive mobility in the cytoplasm and reduced mobility in the nuclei. The reduced mobility concurs with the active role played by Bcd as a transcription factor binding transiently to the DNA (k_{off}=8 s^{-1}). But more importantly, the mobility of Bcd in the cytoplasm is consistent with the SDD model, since we measure an effective diffusion coefficient D ~ 5 μm^2/s. Our work therefore constitutes the first experimentally demonstration that the formation of the Bcd concentration gradient in *Drosophila* embryos is diffusion dependent. By that, we resolved a long lasting discussion about the origins of morphogenetic gradients.

3.2   Materials and Methods

3.2.1   *Drosophila melanogaster* maintenance and embryo sample preparation

Drosophila melanogaster flies expressing *Drosophila* Bcd fused to EGFP were obtained from the laboratory of Eric Wieschaus at Princeton University. The Bcd-EGFP fusion protein was substituted for the endogenous Bcd protein by conducting the mutant crosses of bcd-EGFP with bcd^{E1},p^{P}/TM3,Sb to generate egfp-bcd;bcd^{E1},p^{P} [108]. Flies were maintained at 25°C, to feed and lay eggs. For imaging, live embryos were collected 0-15 minutes after egg deposition. This was followed by embryo dechorionation. Dechorionated embryos were glued on a coverslip (glue dissolved in Heptane) and immersed in halocarbon oil.

3.2.2   Live embryo confocal imaging for N&B analysis

Stacks of time-series confocal images (256x256 pixels, 1000 images/stack) of live embryos expressing Bcd-EGFP were collected at room temperature during the developmental stages 12–14 using the scanning confocal microscope mentioned in part 1 (section 1.4.1 & 1.4.2). Images (78.2x78.2 μm) were collected with a 3.6 μs dwell time (0.694 s/frame), and a 0.305 μm pixel size. These scanning conditions were chosen for photobleaching effect minimization. The detector gain was kept well below pixel saturation level for best nuclear-to-cytoplasmic fluorescence ratio estimates and concentration quantification.

Images were split into different cycles, and the cycles were split into interphase and mitosis stages. Within each stage, stacks of 50 consecutive images (34.7s/50 frames) were analyzed (using the software SimFCS) as a unit to follow the progress of nuclear concentration as a function of time and to minimize the effects of nuclear motion, especially during early interphase. Our choice of 50 frames is reasonable since 50 frames represent ~35 seconds of the embryo lifetime while interphase stages (12-14) last for at least 10 minutes and mitosis for at least 4 minutes. During early interphase, the speed of nuclear motion is rather high as will be seen in later sections. The average concentration and molecular brightness of Bcd-EGFP populations in the nucleus and the cytoplasm were extracted from the concentration-and-

molecular brightness correlation maps, and from line analysis performed on the concentration and the molecular brightness maps.

3.2.3 Line analysis

Multiple vertical and horizontal lines were selected across the concentration map obtained from N&B analysis of live embryos (see Figs. 1 & 2) for relative nuclear and cytoplasmic concentration estimates of Bcd-EGFP. The concentration change during interphase and mitosis was examined throughout cycles 13-14, by selecting the same line for each concentration map. The nuclear-to-cytoplasmic concentration ratio was easily extracted at the single nucleus level as a function of time. Some of the lines were selected at location where interphase nuclei did not form for cytoplasmic amplitude comparison before (mitosis) and after (interphase) nuclei formation. Some of the line analysis captured nuclear motion where the nucleus was clearly displaced at constant rate (v).

3.2.4 Time-lapse imaging

Time lapse movies of embryos expressing Bcd-EGFP were collected at room temperature on the Leica SP5 scanning confocal microscope for nuclei motion analysis. The Argon ion laser, 488 nm line, was used at optimized imaging conditions for high signal-to-noise ratio and minimized photobleaching effects. The glycerin–immersion objective lens (Leica 63x) was used in conjunction with a 320 μm pinhole. Images of 256x256 pixels were collected at 700 line/s scanning frequency. For reducing photobleaching effects even further, the imaging frequency was lowered to 1 image every 3 seconds.

3.2.5 Fluorescence Recovery after Photobleaching (FRAP)

FRAP experiments were performed on the experimental setup described in part 1 (section 1.4.3). Specifically, a circular region (diameter d~2.7 μm) in an anterior nucleus of a living embryo (during cycles 12-14) was photobleached using 100% of the laser's full power for 1 frame (0.387 s/frame). Finally, a small square region (16.8 μm^2) encompassing the photobleached area was imaged to detect fluorescence recovery in and out of the photobleached

region of interest. For comparative reasons and to insure that severe bleaching is not affecting regions outside of the selected area, 50% as well as 30% of laser's full power was also explored. Pre-bleach, bleach, and post-bleach 256x256 pixel imaging was carried out at a 700 lines/s scanning speed and with a 16 nm pixel size. The scanning speed and the size of the photobleached area were adapted from those used for my work on Ran work, so that the recovery time and preponderance of an eventual immobile fraction could be compared between the two proteins.

3.2.6 Fluorescence Correlation Spectroscopy (FCS)

FCS experiments were performed using the home-built system described in part 1 (section 1.4.4). Fluorescein (D~300 μm^2/s, Sigma) was used for confocal volume size calibration before each experiment. From calibration, it was found that ω_0=0.35 μm and z_0=1.75 μm, assuming a Gaussian focal volume. While acquiring measurements (20-40 s/measurement) in live embryos, a low laser intensity power of ~2 μW at the sample was used for fluorescence photobleaching minimization. Photobleaching effects could not be totally eliminated, possibly due to the existence of a population of Bcd protein undergoing very slow dynamics or transient binding. I experimented with lowering the laser intensity power even further, but the signal-to-noise ratio turned out to be too low. FCS measurements where collected at room temperature, which is ideal for the development of *Drosophila* embryos. Measurements were carried out in the anterior nuclei and cytoplasm during interphase of the developmental stages 10-14.

The analysis of the autocorrelation functions (ACF) is detailed in part 1 (section 1.4.4). Briefly, two models were used to retrieve dynamics and concentration parameters from the nuclear and cytoplasmic FCS data. First, a 2-component diffusion model (Eq. (1.4.4.1), n=2, B=0) was used to fit the autocorrelation function in order to account for a visible slow dynamical term present in the ACFs collected. The aspect ratio retrieved from the calibration, S=5, was fixed during this analysis and in this case the constant C was fixed to zero. All other parameters were left as variables to be extracted from the least-square fit.

To separate possible nuclear motion contributions to the ACF at longer time scales, a 3-component diffusion model (Eq. (1.4.4.1), n=3, B=0) was used to re-analyze all ACFs with

unusually long characteristic diffusion time for the second term ($\tau_{D,2}$). This procedure is explained further in the results part.

The Pearson correlation coefficient, r, was calculated to test the hypothesis of the lack of correlation between $\tau_{D,1}$ and $\tau_{D,2}$ for pairs of data points with $\tau_{D,2} < 0.1$ s (n=105), and for those with $\tau_{D,2} > 0.1$ s (n=117).

As a second model, the stick-and-diffuse (SAD) model was used to capture the possible transient binding of Bcd-EGFP to the DNA in the nucleus and determine the binding (k_{on}) and unbinding (k_{off}) rates associated with that process. A detailed description of the definition of the model and the parameters recovered from the fit can be found in part 1 (section 1.4.4). The model was used to analyze the average ACF of all nuclear Bcd-EGFP measurements with $\tau_{D,2} \leq 0.1$ s but with the exception of those ACFs that contained a third component that is related to the slow nuclear motion.

Again, least-square fitting to the two models was performed using the KaliedaGraph and Maple softwares, respectively. Four independent parameters where varied during the fit for the 2-component diffusion model (A_1/N, A_2/N, $\tau_{D,1}$, $\tau_{D,2}$), as well as for the stick-and-diffuse model (N, τ_D, k_{on}, k_{off}).

Although EGFP exhibited photophysical fluorescence blinking in the ACFs recorded in the nucleus and the cytoplasm of *Drosophila* embryos expressing Bcd-EGFP, the blinking term was excluded by cutting all FCS curves at a time slower than the blinking time (1 ms) when analyzing the dynamical behavior of Bcd. The choice of a time scale to cut at is based on curves that exhibited very clear blinking effects. The exclusion of the blinking term was done because of the difficulty to fit it for some individual FCS curves when using the 2-component diffusion model. Since the measurement time was only ~20 seconds (to avoid fluorescence photobleaching), the signal-to-noise ratio did not allow us to fully fit this term in some ACFs.

3.3 Results

3.3.1 Spatial and temporal distribution of the protein Bcd-EGFP in live *Drosophila melanogaster* embryos during developmental stages 13–14

We revisited the concentration gradient analysis done by Gregor et al. [113] using different imaging conditions and a different method for the estimate of the absolute concentration of Bcd. First, we used one-photon excitation as opposed to the two-photon excitation used in this earlier study. Second, we used correlation spectroscopy techniques instead of average fluorescence intensity measurements to estimate concentration. We measured the gradient in both the cortical nuclei and cytoplasm along the dorsal and ventral sides of the embryo.

A typical confocal intensity image of live *Drosophila melanogaster* embryo expressing Bcd-EGFP during the mitosis of cycle 13 and during early interphase of cycle 14 are shown in Fig.17A & Fig. 18A, respectively. During the mitosis of cycle 13, a fluorescence intensity gradient along the dorsal cortical cytoplasm is evident, with Bcd-EGFP residing preferably at the anterior (Fig. 1A). The cytoplasmic intensity distribution exhibited a clear exponential decay with a decay length of ~100 μm (see Fig. 24), similar to the reported dorsal nuclear intensity decay [113]. This distribution was conserved during interphase of cycle 14 with a cytoplasmic amplitude loss of ~ 20%, due to the concentration of Bcd in the nuclei. An anterior nuclear-to-cytoplasmic fluorescence intensity ratio (I_N/I_C) of ~12–15 was recovered during the interphase of cycle 14. This ratio is at least three times higher than what has been reported by Gregor et al [108].

In order to obtain the absolute concentration profile of Bcd along the dorsal nuclei and cytoplasm, and to probe environmental differences that could affect the detected fluorescence intensity measurements leading to artifacts in concentration estimates, we used N&B analysis Two representative examples are shown in Fig. 17 & Fig. 18. The average fluorescence intensity map of an embryo expressing Bcd-EGFP (in mitosis of cycle 13 and interphase of cycle 14, Fig. 17A & Fig. 18A respectively) was split into its two contributing parameters maps: the average number of molecules map (Fig. 17C & Fig. 18C) and a molecular brightness map (Fig. 17D &

Fig. 18D). During mitosis, the molecular brightness of the EGFP fluorophore is strikingly uniform throughout the embryo, including regions around the chromatin where the concentration of Bcd is slightly higher than in the rest of the cytoplasm (Fig. 19D). In interphase, the molecular brightness of EGFP fluorophore is still very uniform throughout the cytoplasm (and equal to its molecular brightness in mitosis), but in regions around the nuclei it seems ~1.5 times higher (Fig. 18D). We discuss below the possibility that this is due to environmental differences between the nucleus and the cytoplasm (see section 3.3.5). When comparing the correlation maps in Fig. 17B & Fig. 18B, one can see that, when disregarding pixels outside the embryo, only one pixel population is present in mitosis, whereas two pixel populations, distinguished by different EGFP-Bcd concentration and molecular brightness, are present in interphase. One (with the lower concentration and molecular brightness) corresponds to pixels in the cytoplasm, and the other corresponds to pixels in the nuclei. The concentration map visually confirmed that Bcd-EGFP is non-uniformly distributed along the dorsal side of the embryo, highly accumulating in the anterior nuclei (Fig. 18C) and cytoplasm (Fig. 17C). An average anterior nuclear-to-cytoplasmic C_N/C_C concentration ratio of ~8-10 during interphase was extracted from the correlation map (Fig. 18B) by comparing the brightness versus concentration value at the center of the two populations. This value was confirmed from intensity line analyses applied across anterior nuclei and portion of the cortical cytoplasm of the concentration map (Fig. 19).
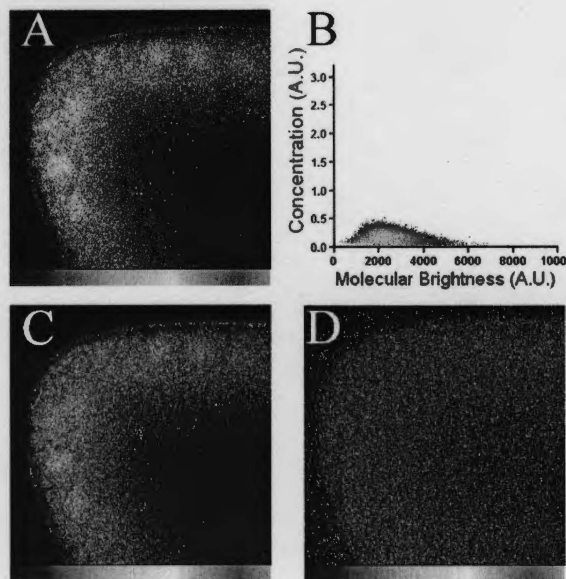
Figure 17. Spatial distribution of Bcd-EGFP during the mitosis of cycle 13. (A) Average intensity map for an embryo expressing Bcd-EGFP. (B) Correlation between the average Bcd-EGFP concentration and molecular brightness at each pixel. Only one Bcd population is apparent during mitosis with uniform molecular brightness. (C) Concentration map. (D) Molecular brightness map. A uniform molecular brightness is evident throughout the cytoplasm. Image size: 78.2x78.2 μm^2.
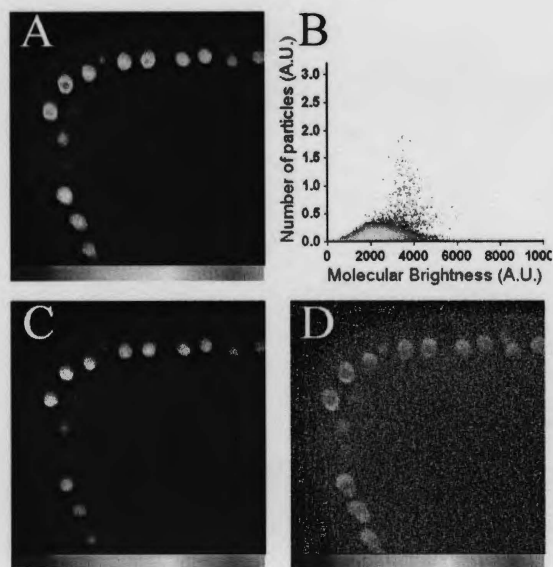
Figure 18. Spatial distribution of Bcd-EGFP during the interphase of cycle 14. (A) Average intensity map. (B) Correlation between Bcd-EGFP average concentration and molecular brightness at each pixel. A second pixel population emerges during interphase, with higher concentration and higher molecular brightness, corresponding to the nuclei. (C) Concentration map. The protein is highly concentrated in the nuclei. (D) Molecular brightness map. EGFP is ~1.5 times brighter in the nuclei than that in the cytoplasm, with the highest brightness in nuclear regions closest to the nuclear envelope. Image size: 78.2x78.2 μm^2.
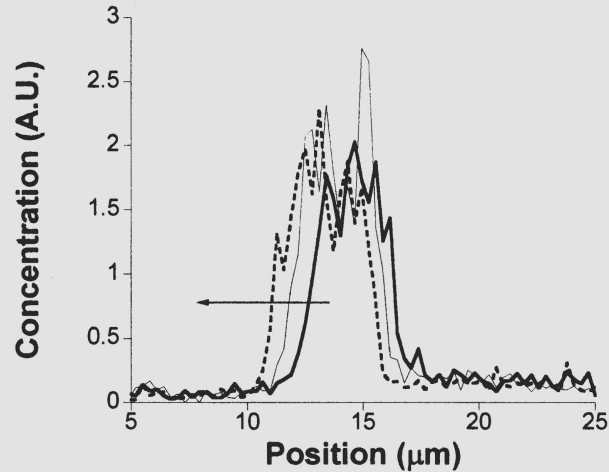
Figure 19. **Anterior nuclear-to-cytoplasmic concentration ratio of Bcd-EGFP in interphase**. Line analysis was applied to concentration maps, each obtained from the analysis of 50 consecutive frames (~35 s/50 frames). A relative nuclear-to-cytoplasmic concentration ratio of ~ 10 is demonstrated in this figure, and a nuclear motion occurring at a speed of ~ 1.2 μm/minute has been calculated.

3.3.2 Motion of nuclei

Time lapse imaging of the embryos during the developmental stages 10-14 revealed a continuous nuclear motion with different velocities at each stage. Tracking of the nuclei position was done on a time-series of confocal images to estimate this nuclear velocity. Nuclei are found to be fast moving during early interphase of cycles 9–14 with a velocity of 12 ± 4 μm/min with a full range of motion along the dorsal side of the embryo (movie 1), comparable to that reported for nuclei undergoing migration [114]. During mid-interphase cycles, nuclei velocity is reduced to 1.2 ± 0.6 μm/min and the range of motion is reduced to a few microns (movie 1). This motion was also captured through the line analysis done to estimate the anterior nuclear-to-cytoplasmic concentration ratio. Fig. 19 shows a nucleus moving with a velocity of ~1.2 μm/min during mid-interphase. A third type of motion that was noticed is a fast in-plane "wiggling" motion on top of the directed motion during early- and mid-interphase. The rate of this latest motion was hard to estimate due to time resolution limitations imposed by the imaging rate of one image every 3

seconds, which was chosen to minimize fluorescence photobleaching effects. The effects of these motions on the Bcd dynamics measured by FCS will be discussed in a later section.

3.3.3 Mobility of nuclear Bcd-EGFP using FRAP

Direct photobleaching experiments have already been employed to explore both the cytoplasmic Bcd dynamics and the nucleo-cytoplasmic Bcd concentration equilibrium dynamics [108] in live embryos expressing Bcd-EGFP during the mitosis of cycle 13. The nuclear dynamics of Bcd on the other hand had not yet been investigated. Here we use one-photon fluorescence recovery after photobleaching (FRAP) to assess the possible existence of an immobile nuclear Bcd-EGFP fraction during interphase in cycles 12-14. Fig. 20 shows a normalized fluorescence recovery trace corresponding to the average of 24 separate measurements taken in the anterior nuclei of 5 different embryos, all during cycles 12-14. A 100% fluorescence recovery is clearly visible, and was consistently obtained for each individual recovery trace once it had been normalized to the fluorescence intensity in an adjacent unbleached region. Fluorescence intensity equilibrium between the bleached and unbleached regions is reached within a few seconds. This is an indication of the dynamic behavior of nuclear Bcd, including a total absence of an immobile fraction. This result is expected for transcription factors and other chromatin-binding proteins [17][16][15]. An average half-time for recovery of 1.1 ± 0.4 s was obtained. No difference in recovery time was noticed throughout the developmental stages 12-14; indicating early maturation and stability of the dynamic behavior of nuclear Bcd. On top of the fast ~1s equilibration dynamic, a long-range recovery time of 60 ± 30 s was noticed in some of the recovery traces (data not shown). This is not surprising, since ~ 70 ± 20 s is the time that Gregor et al. reported was necessary for the nuclear and cytoplasmic fraction of Bcd to equilibrate [108].
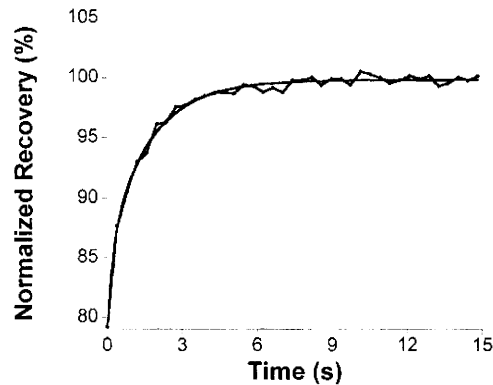
Figure 20. The average fluorescence recovery after photobleaching (FRAP) trace of Bcd-EGFP in anterior nuclei of different embryos throughout stages 12-14. Blue: Average nuclear fluorescence recovery trace of Bcd-EGFP after photobleaching (1 frame, 0.387s/frame) in circular regions ($5.7\mu m^2$). Black: single-exponential fit to the data. An average recovery time $\tau_{1/2}=1.1\pm0.4$ s is retrieved from that fit. The 100% recovery of fluorescent Bcd in the bleached area is an indication of the lack of permanently immobilized Bcd proteins.

3.3.4 Mobility of Bcd-EGFP in the nucleus and cytoplasm using FCS

Single-point fluorescence correlation spectroscopy (FCS) is a well-established non-invasive technique with a capacity for detecting fast dynamics of fluorescent molecules in live systems. To study the cellular dynamics of Bcd-EGFP, we performed 280 separate FCS measurements in anterior nuclei (255 measurements) and cytoplasm (22 measurements) of 8 different embryos during the interphases of cycles 12-14 (Fig. 23A). The autocorrelation functions (ACF) obtained for Bcd-EGFP could not be explained by the diffusion of one single species, but instead most of them contained at least two visible contributions: a term consistent with a fast diffusive motion, and a term corresponding to a noticeably slower dynamics. Some curves contained a third term that corresponded to a very slow motion. To gain insight into the molecular processes causing this dynamics, we analyzed the data with two different models: the 2-component diffusion model and the stick-and-diffuse model (See materials and methods).

The 2-component diffusion model assumes that all detected species of the fluorescent protein are undergoing independent diffusive motion with a residence time τ_n in the confocal volume. To test this assumption, all ACF were analyzed with a two-component diffusion model

with τ_1 and τ_2 residence times for the fast and slow dynamic species, respectively. The correlation coefficient between τ_1 and τ_2, r, was calculated. Fig. 21B shows the value of r calculated as a function of the maximum value of τ_2. According to this calculation, the residence time of the two most dominant components (τ_1 and τ_2) were not correlated (r=0.2±0.1) when τ_2 was less than 0.1 seconds. Notice that the correlation coefficient, r, for this population of data is constant. On the other hand, when τ_2 was greater than 0.1 seconds, the correlation between τ_1 and τ_2 increased until it reached a plateau at r=0.67. Fig. 21C shows a correlation map between τ_1 and τ_2 with the poorly correlated population marked blue, and the highly correlated one marked black. We suspect that the high correlation observed in this second population of curves is due to the interference by the nuclei motion which might increase both apparent residence times τ_1 and τ_2 in a correlated manner. This hypothesis was tested by re-analyzing some of these curves with a 3-component diffusion model instead in order to account for this slow drifting motion, which resulted in lowering the value of the residence time τ_2 to less than 0.1 seconds and dramatically reducing its correlation with τ_1. In cytoplasmic measurements on the other hand, a third population was not noticed and the value of τ_2 was well below 0.1 seconds. A correlation coefficient r=0.38 was found between cytoplasmic τ_1 & τ_2.

When all nuclear data was included with no exclusion of any ACF (255 measurements), 50% of the Bcd-EGFP population was undergoing fast diffusive motion with apparent D_{app}=7.0±4.7 $\mu m^2/s$, and the remaining population was undergoing a slow motion with D_{app}=0.26±0.31 $\mu m^2/s$. The correlation coefficient of this set of data was found to be r=0.67.

Nuclear data with τ_2<0.1 s (with the exclusion of ACFs that had to be re-analyzed with the 3-component diffusion model) were selected for further analysis. When analyzing all ACFs individually using this model, the majority of the signal from cytoplasmic Bcd-EGFP (~70%) corresponded to molecules diffusing with a diffusion coefficient of D=5.2±2.3 $\mu m^2/s$ (12 ACFs). The remaining 30% of the Bcd-EGFP was undergoing a much slower motion with D=0.53±0.56 $\mu m^2/s$. In contrast, in the nucleus (103 ACFs), the contribution of the slowly moving Bcd-EGFP molecules (D=0.31±0.21 $\mu m^2/s$) represented 51% of the signal, while the fast mobility of the remaining 49% of Bcd-EGFP (D=9.5±4.7 $\mu m^2/s$) was consistent with a freely diffusing

population of the Bcd protein. These results are summarized in Fig. 22 where diffusion coefficient histograms were generated for individual nuclear and cytoplasmic Bcd-EGFP. (Average D values mentioned above are weighted averages and errors are SDs).

To further investigate the biological significance of the slow fraction of Bcd in the nuclei, and considering the likely possibility that this slow fraction corresponded to molecules transiently binding to the DNA, we analyzed the average ACF with the stick-and-diffuse model [13]. As mentioned in the materials and methods section, this model assumes an even distribution of one type of immobile binding sites with a binding rate k_{on} and unbinding rate k_{off}, where Bcd diffuses freely between two consecutive binding events with a diffusion coefficient D. These assumptions are in good agreement with the biological function of Bcd as a transcription factor transiently binding to the DNA, and with the existence of two independent uncorrelated dynamic terms in the ACF. The model was applied to the ACF obtained by averaging all the measurements recorded in nuclei (Fig. 23) with $\tau_2 < 0.1$ seconds (at the exclusion of ACFs that had to be re-analyzed with the 3-component diffusion model) (103 ACFs in total). The best least-square fit corresponded to a binding rate $k_{on} = 4.4$ s^{-1} and to an unbinding rate $k_{off} = 8.3$ s^{-1}. Thus according to this analysis, at any time 35% of nuclear Bcd-EGFP is bound to an immobile nuclear structure, presumably chromatin. The diffusion coefficient retrieved for the free Bcd-EGFP using this model is ~ 4 $\mu m^2/s$, a reasonable value for a freely diffusing protein with the size of Bcd-EGFP ($MW_{Bcd} \sim 55$ kDa [100]) when compared to that of freely diffusing EGFP in the same embryos ($MW_{EGFP} \sim 29$ kDa, $D \sim 6$ $\mu m^2/s$). The observed 30% decrease in the diffusion coefficient of Bcd-EGFP in comparison to that of EGFP is expected if size effect is the only factor to play a role in the Bcd diffusion coefficient determination. A summary of all the results from the analysis of our Bcd-EGFP FCS measurements can be found in table 2. The fit of the stick-and-diffuse model to the average nuclear Bcd-EGFP ACF is more statistically significant than that of the 2-component diffusion model, as seen from the corresponding χ^2 values.
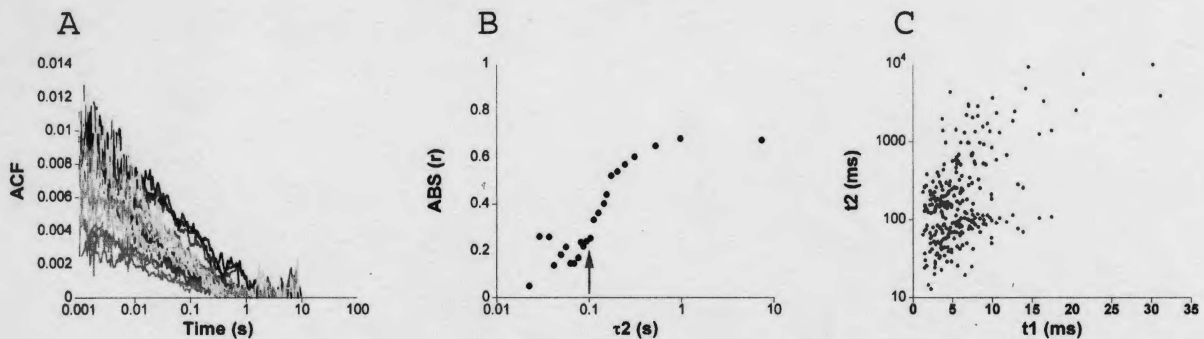
Figure 21. Distribution of characteristic diffusion times of Bcd-EGFP in the anterior nuclei.
(A) Representative nuclear ACF curves with different amplitudes. (B) The absolute correlation coefficient, r, calculated as a function of the maximum value of τ_2. Low and constant correlation (r=0.2) was found when τ_2<0.1 s. When τ_2>0.1 s, the correlation coefficient increased exponentially until reaching a Plato at r=0.67. The red arrow marked the change in correlation behavior. (C) The τ_1 and τ_2 correlation map. The correlation map is divided into a low correlation population (blue) with a correlation coefficient r=0.2 and a high correlation population (black) with a correlation coefficient r=0.67. The two populations are divided at τ_2=0.1 s.
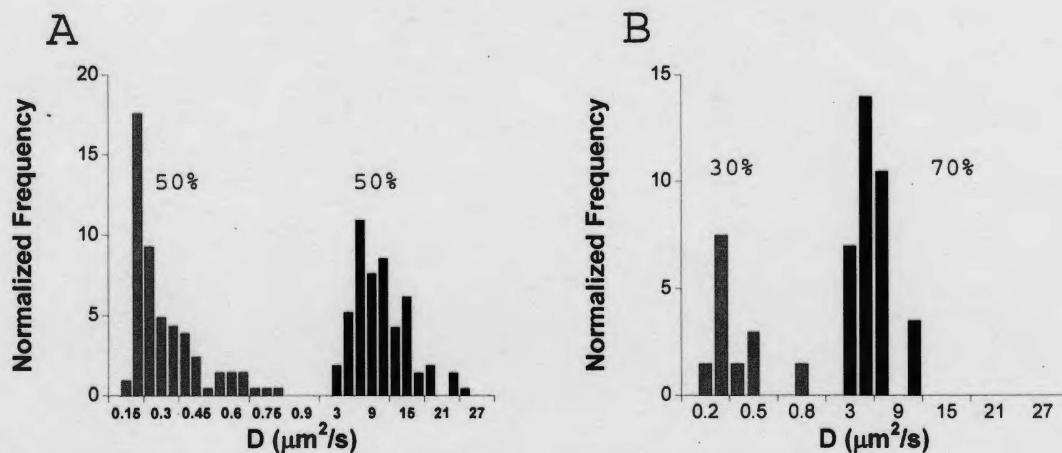
Figure 22. Distribution of diffusion coefficients of Bcd-EGFP in the nuclei and cytoplasm.
Black columns correspond to the fast dynamical processes and gray columns to the slow dynamics. The total occurrence for each process has been normalized to its average relative weight in the correlation function. (A) Diffusion coefficients obtained for Bcd-EGFP in the anterior nuclei of embryos during interphase of cycle 10-14. (B) Diffusion coefficients obtained for Bcd-EGFP in the cytoplasm during interphase of cycle 10-14. All data in this figure have been obtained for a laser power at the sample I=2 µW.

66
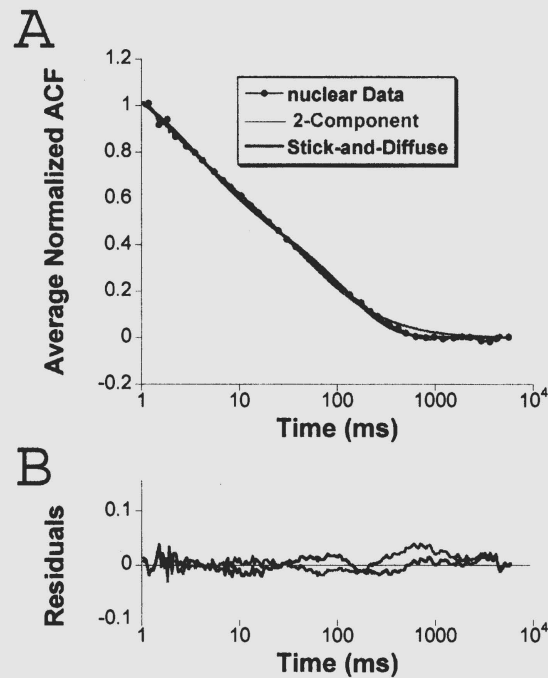
Figure 23: Analysis of the average autocorrelation function obtained for nuclear Bcd-EGFP with the 2-component diffusion model and the stick-and-diffuse model. (A) Nuclear Bcd-EGFP data (filled black symbols), fit to the 2-component diffusion model (red line) and to the result of the stick-and-diffuse model (blue line). The corresponding residuals are shown in (B) with respective line color to the fit in (A). The stick-and-diffuse model resulted in a better fit to the Bcd-EGFP FCS data.

Model	$D_1(\mu m^2/s)$	$D_2(\mu m^2/s)$	$A_1(\%)$	$A_2(\%)$	k_{on} (s^{-1})	$k_{off}(s^{-1})$	χ^2
2-component (Nucleus)	9.5	0.3	49	51	-	-	0.045
Stick-and-diffuse (Nucleus)	3.95	-	65	35	4.4	8.3	0.026

Table 2: Summary of the results obtained from the two models used to fit the nuclear Bcd-EGFP FCS data. The parameters for the 2-component diffusion models are defined in Eq. (1.4.4.1). Those for the stick-and-diffuse model are defined in Eq. (1.4.4.4). χ^2 is the chi square value with the weight for all data points set to 1.

3.3.5 Fluorescence blinking of EGFP

A term accounting for the blinking process of the EGFP chromophore was included in the autocorrelation analysis (see methods). Two parameters were recovered from this analysis, the blinking relaxation time (τ_B) and the ratio of non-fluorescent molecules due to protonation (blinking ratio, B). While the nuclear and cytoplasmic blinking relaxation times retrieved were equal ($\tau_B=300$ µs), a higher fraction of EGFP in the dark protonated state was found in the cytoplasm when compared to that in the nucleus ($B_C=0.28\pm0.05$ & $B_N=0.15\pm0.04$). The cytoplasmic-to-nuclear blinking ratio is ~1.9, which translates to 1.9 times brighter EGFP in the nucleus when compared to that in the cytoplasm. This is in agreement with the N&B analysis (Fig. 18B & 18D) where nuclear-to-cytoplasmic molecular brightness ratio of 1.5 was recovered. The difference in molecular brightness of EGFP (due to blinking) in the main embryonic compartments is indicative of the different environments Bcd is exposed to in the nuclei and the cytoplasm. The implications of environmental differences and its effects on Bcd will be discussed in the discussion section of this study.

3.3.6 Bcd concentration profile

Fluorescence correlation spectroscopy (FCS) is an ideal technique for the determination of both dynamics and absolute concentration of fluorescent molecules in live systems. Absolute concentration measurements of Bcd-EGFP in the anterior nuclei of the developmental stages 10-14 are possible when photobleaching effects are minimized by using low laser excitation power. Photobleaching effects can be further reduced by considering only the first few ACF measurements recorded. Assuming uniform molecular brightness of EGFP throughout the nucleus, the amplitude of the ACF corresponds to the inverse of the average number of Bcd-EGFP molecules in the confocal volume. N&B analysis showed a uniform molecular brightness for Bcd-EGFP protein whether undergoing diffusive motion or transient binding in the center of the nuclei, where the FCS measurements were recorded. The ACF amplitude $G(0)=(A_1+A_2)/N=1/N$ (Eq. (1.4.4.1), n=2, B=0), where $A_i=N_i/N$ for the ith specie and $N_1+N_2=N$. On average ~250 molecules were occupying a confocal volume of 2.7 μm^3 in the most anterior

nuclei during the different developmental stages. This corresponds to an anterior Bcd concentration of at least 120 nM.

Given the absolute concentration of Bcd in the anterior nuclei (120 nM), the concentration profile of Bcd with a decay length $\lambda \sim 100$ µm over an embryo length of 480 µm, and the nuclear-to-cytoplasmic concentration ratio, the nuclear/cytoplasmic concentration profile can be easily calculated (Fig. 24).

A

B
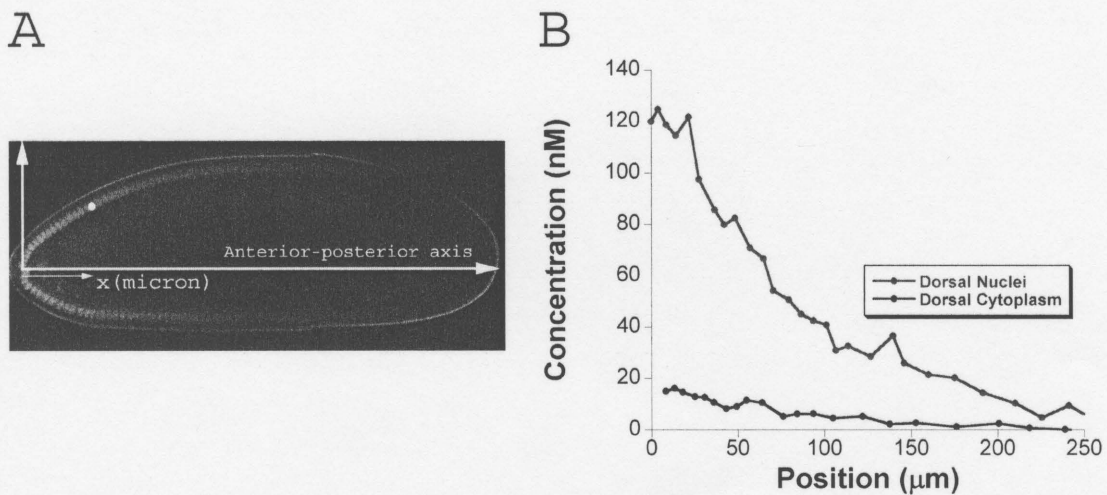
Figure 24: The absolute concentration profile of endogenous Bcd in Drosophila melanogaster embryos during interphase of cycles 9-14. Nuclear and cytoplasmic Bcd protein concentration profiles were extracted from confocal images of live embryos expressing Bcd-EGFP using the software ImageJ and from FCS measurements. (A) Confocal Image of live embryo expressing Bcd-EGFP in early interphase of cycle 14. Image courtesy of Aude Porcher. Circular window of the size of a nucleus was manually moved along the outer edge of the embryo to sample the fluorescence intensity profile in cortical nuclei and cytoplasm. The average intensity within each window was plotted versus the x-position along the anterior-posterior axis. Similar analysis was carried out along the cortical cytoplasm and in close proximity to the nuclei to determine Bcd cytoplasmic intensity profile. (B) Bcd-EGFP nuclear and cytoplasmic concentration profiles along the embryo. The absolute concentration values at the anterior tip of early embryos through the different interphase cycles was retrieved from multiple FCS measurements. The nuclear concentration at the anterior was found to be ~120 nM, and that of the anterior cytoplasm is estimated to be 15 nM. The nuclear/cytoplasmic exponential profile plot had a 120/15 nM amplitude and the reported decay length $\lambda \sim 100$µm. The total length of the embryo is 480 µm.

3.4 Discussion

3.4.1 Molecular brightness of EGFP in live *Drosophila* embryos

The N&B analysis performed on movies of live Drosophila embryos showed a surprising difference in the molecular brightness of Bcd-EGFP between the nuclei and the cortical cytoplasm, with the molecular brightness of the fluorescent molecule being on average 1.5 times higher in the nuclei. At this point, it is worth pointing out that the "molecular brightness" measured by fluorescence fluctuation techniques, including N&B analysis, is the average fluorescence photon flux detected per diffusing molecular unit. Therefore, if a fluorescent protein oligomerizes, its molecular brightness increases. Such an increase was measured for example in the case of the oligomerization of several receptors [116]. Another reason why the molecular brightness of a molecule might change is if the "environmental" conditions in which the fluorophore finds itself change. For example, it has been shown that the molecular brightness of EGFP is strongly dependent on the acidity, ionic strength, viscosity and temperature of the buffer, [23, 117]. This dependence on environmental parameters can be attributed to the equilibrium that exists between two different forms of EGFP: in its low-pH protonated form EGFP is not fluorescent, while in its high pH de-protonated form EGFP it is. At intermediate pH, each protein constantly alternate between these two forms, which gives raise to the well known blinking observed for EGFP and its derivatives.

In our case, the FCS experiments that we performed independently allowed a direct observation of the blinking of the protein. We found that on average only 15±4% of EGFP molecules were in the non-fluorescence protonated state in the nuclei, against 28±5% in the cytoplasm. Therefore the change in the blinking characteristics between nuclei and cytoplasm might be sufficient to explain why the detected molecular brightness of EGFP is higher in the nuclei. It is not absolutely obvious how much the molecular brightness should change given the measured change in the fluorescent fraction of the protein, because moment analysis might fail to take into account the blinking of the fluorophores properly if the relaxation time of the blinking (~300 μs) is too long compared to the line-to-line return time (~2.7 ms). This is a fine point, which will need to be further investigated, for example by measuring the molecular brightness of

EGFP solutions at different pH both using N&B analysis in different conditions and the blinking parameters recovered by FCS.

In conclusion, since we measured a change in blinking characteristics in agreement with the change in molecular brightness, and since Bcd is not known to form homo-oligomers, the most likely explanation for the high the molecular brightness of the fusion protein in the nuclei is that there it finds itself in very different environmental conditions than in the cytoplasm. In general, pH, viscosity, ionic strength and temperature should be the same in both compartments (for example, the molecular brightness of EYFP, as we have seen in part 2 of this thesis, is not affected by its nuclear vs. cytoplasmic location in HeLa cells). It is therefore tempting to conclude that a molecular process specifically involving Bcd is taking place in the nucleus, and that this molecular process results in a significant change in environment for the attached fluorophore. Two such processes can be immediately thought of. The first is binding of Bcd to its target regulatory sequences on the DNA. Binding to a charged molecule such as DNA could results in a change in local ionic strength for the fluorophore. The second is specific degradation of Bcd, which would involve binding of the protein to molecular structures such as proteasomes which are devoted to the degradation of other proteins [118] and present at high concentration in the nuclei [119], and in which extreme environmental conditions may be found. This second possibility is particularly exciting, because it was recently proposed, based on scaling arguments for fly embryos of different sizes, that Bcd degradation (which with diffusion is the other tenet of the SDD model) must occur in the nuclei [111].

This remains very tentative, and several different controls could be done to support these ideas. For example, lifetime measurements could give an independent verification that the environmental conditions sensed by the flurophore are very different in the nucleus. And importantly, a control experiment with the free EGFP fluorophore (as was done with EYFP as a control for EYFP-Ran) could determine whether environmental conditions are indeed the same in the nuclei and cytoplasm of *Drosophila* embryos, and establish that the increase in molecular brightness we observe is specific to Bcd. If available, mutants of Bcd that do not bind to DNA could be used to rule out interactions with DNA as a cause for the detected environmental change.

3.4.2 Localization of Bcd in *Drosophila* embryos

The N&B analysis allowed us determining a concentration ratio $C_N/C_C \sim 8$ in early interphase of cycle 14 along the anterior-posterior axis after correcting for the effects of the varying molecular brightness across the embryo, and confirmed the exponential-like nuclear and cytoplasmic concentration gradients. On the other hand, FCS measurements at the anterior pole enabled us to extract the absolute nuclear concentrations $C_N = 120$ nM, and therefore the absolute cytoplasmic concentration, $C_c = 15$ nM. Taking N&B analysis results together with that of FCS, an estimate for the absolute nuclear and cytoplasmic concentration profiles was extracted as seen in Fig. 10B.

Our nuclear concentration at the anterior ($C_{anterior} \geq 120$ nM) is 2-folds higher than that reported by Gregor et al. ($C_{anterior} = 55$ nM) [108]. This discrepancy could be due to several different causes. There could be two sources of systematic error in our experiments, each acting in a different direction. First, as mentioned in the materials and methods, fluorescence photobleaching was not totally suppressed while recording the FCS data in spite of all our efforts. Therefore the measured concentration could be an underestimate, i.e. the discrepancy with the results of Gregor et al. could be even higher. On the other hand, background fluorescence such as can be expected in living organisms always causes the amplitude of the correlation function, and results in an overestimate of the concentration. However, a 2-fold error due to fluorescence background seems unlikely given the good quality of the FCS data obtained in the nuclei. The estimate of Gregor et al. is based on the assumption that the molecular brightness of EGFP in the nucleus is equal to that in solution, and on the recording of calibration curves from known concentrations of EGFP in solution. In other words, their estimate is based on the assumption that fluorescence intensity is equivalent to concentration. Although this might very often be the case, we have demonstrated using both N&B analysis and FCS that this was not true in the case of Bcd-EGFP in *Drosophila* embryos. Depending on the difference in brightness for EGFP between the solutions used for calibration and the embryos nuclei, this could lead to either an overestimate or underestimate of the concentration. In addition, fluorescence photobleaching effects, which are known to be especially severe in the detection volume of 2-

photon confocal microscopes [120] and when long exposure times are used, could be a factor. Photobleaching will always lead to an underestimate of the protein concentration, and would explain why we measure a 2-fold higher concentration.

Gregor et al. measured a nuclear-to-cytoplasmic fluorescence intensity ratio of $I_N/I_C \sim 4$, while we measured a much higher ratio with $I_N/I_C \sim 12$ using fluorescence intensity analysis. This discrepancy between the two studies could again be due to the above mentioned photobleaching effects, which should be more severe in compartments with high fluorescent protein concentration. This hypothesis could easily be tested by measuring the I_N/I_C ratio as a function of laser intensity.

The distribution of Bcd-EGFP in the cytoplasm clearly followed a simple exponential trace along the embryo's dorsal side with similar decay length to that reported along the dorsal nuclei. Gregor et al. have demonstrated that the Bcd-EGFP fluorescence intensity is stable through the interphases of cycles 10-14 [108], where at the beginning of each of these cycles the Bcd fluorescence intensity in a nucleus is equal to that measured at the beginning of the previous interphase cycle in an adjacent nucleus. Since the cytoplasmic concentration profile of Bcd was constant between mitosis of cycle 13 and interphase of cycle 14 (Fig. 17C & 18C), I conclude that the nuclear and cytoplasmic concentration profiles of Bcd is the same throughout stages 10-14 (Fig. 24).

It is worth noticing the uneven concentration distribution of the protein around disintegrating nuclei during mitosis. This localization was noticed for other DNA binding proteins [55].

3.4.3 The mobility of Bcd in the nuclei is consistent with its role as a transcription factor

In the nucleus, the mobility of Bcd seemed to be due to the interplay between two different processes: a fast diffusive process characterized by $D \sim 9.5$ $\mu m^2/s$, and a slower dynamical process that we attribute to transient binding to the chromatin with characteristic binding rate of $k_{on} = 4.4$ s^{-1} and unbinding rate $k_{off} = 8.3$ s^{-1}. Therefore, on average, 35% of

nuclear Bcd is engaged in transient binding at all times. This finding is consistent with the protein's primary function as a transcription factor transiently interacting with the DNA. This association could explain Bcd apparent localization in the proximity of the mitotic locations of nuclei after the degradation of the nuclear envelope (as seen in Fig. 17), although we have seen that this was unlikely for Ran. Only a more precise analysis of the dynamics of the protein around the nuclei just after the permeabilization of the nuclear envelope will allow answering this question. I just started working on nuclear envelope degradation visualization with respect to the disappearance of nuclear Bcd using mutant embryos expressing Nup50-mRFP fusion protein together with Bcd-EGFP. This mutant was provided to us by our collaborator Nathalie Dostatni, and it facilitates the localization of the nuclear envelope during Interphase stages. Since transient interactions of any nuclear protein with the chromatin is limited by the availability of the freely diffusing population of that protein, it is not surprising that a large population of nuclear Bcd (65%) was found to be freely diffusing.

3.3.4 Bcd cytoplasmic mobility is consistent with the SDD model

According to the SDD model and the two observables (λ~100 µm & $\tau \geq$90 minutes) that are dependent on the cytoplasmic diffusion coefficient of Bcd, a diffusion coefficient of at least 2 $\mu m^2/s$ is required to validate the model. According to our FCS results in the cytoplasm of early embryos, the amplitude of the autocorrelation term corresponding to freely diffusing Bcd represented ~70% of the total amplitude. The corresponding diffusion coefficient for this fast process (D=5.2±2.3 $\mu m^2/s$) was only ~13% lower than that of the freely diffusing EGFP in the same embryos [111]. Even if we take into account the very slow mobility of the remaining Bcd-EGFP proteins (D=0.53±0.56 $\mu m^2/s$), the average mobility of cytoplasmic Bcd-EGFP, according to our measurements, is still D ~ 3.8 $\mu m^2/s$. The actual diffusion coefficient of endogenous wild-type Bcd should be, if anything, slightly higher than that. Our results in the cytoplasm then confirm that cytoplasmic Bcd is mobile enough to form the observed morphogen gradient by diffusion alone, and validate the commonly used model to explain the origins of the Bcd concentration gradient.

This result is in direct contradiction with the results reported in a recent study by Gregor et al., where the authors used both FRAP and theoretical calculations to estimate the diffusion coefficient of Bcd-EGFP, which they found to be on the order of 0.3 $\mu m^2/s$ [108]. We argue here that both the methods they used to reach this estimate are flawed, and will lead to an underestimate of the diffusion coefficient of Bcd. Firstly, under the experimental conditions used to carry out their confocal FRAP experiments, where they used a large photobleaching area (16x16x7 μm^3), Gregor et al. only captured the slower dynamics of Bcd, just as we did when using confocal FRAP in this part of the thesis and in part 2, even though we used a smaller bleaching area. This is hardly surprising since confocal FRAP is known for its inability to capture fast dynamics [12, 24]. The reason behind that is rather simple. A pixel-by-pixel scanning is required for both bleaching and fluorescence recovery tracing. The long time required for performing efficient bleaching of the selected area is considerably longer than the time needed for fast moving particles to diffuse back to the bleached region of interest. Only the tail of the fast process is often recorded in the recovery trace, which makes it hard to extract accurate diffusion coefficients corresponding to the fast dynamical process. Since the fast process is mostly missing from the confocal FRAP recovery trace, only slower dynamics can be retrieved [24]. The agreement between the diffusion coefficient of the slow population we extracted from the nuclear and cytoplasmic FCS data (D=0.3-0.5 $\mu m^2/s$) with that retrieved from confocal FRAP done by Gregor et al. (D=0.3 $\mu m^2/s$) [108] supports this conclusion. Secondly, when carrying out their theoretical estimate of Bcd diffusion coefficient based on the rate of nucleo-cytoplasmic import of the protein, Gregor et al. make the assumption that every collision event between a Bcd protein and a nucleus results in nuclear import. This is obviously an overestimate of the efficiency of nuclear import, since the coverage of the nuclear membrane by nuclear pore complexes is far from 100%, and since it is well known from single-molecule nuclear import measurements that there is a high rate of "missed" events where nuclear cargoes do not completely go through the nuclear pore complexes [121]. Because the rate of nucleo-cytoplasmic measured by Gregor et al depends linearly both on the diffusion coefficient of Bcd and on the "rate of success" of nuclear import after a collision, overestimating the latter results in an underestimate for the former. The authors struggled to explain how a very slow dynamics of

Bcd in the cytoplasm could establish a stable concentration gradient within the time frame of development. Our results, by reinstating diffusion as the main player in the establishment of the gradient, solve this problem.

3.5   Conclusions & Perspectives

In 1970, Crick proposed a model in an attempt to mathematically test the possibility of forming a morphogen concentration gradient along a developing embryo of 50 cells within the development time frame [80]. He simply proposed that if a morphogen is capable of undergoing diffusive motion from the source of production to the opposite end of the embryo, a concentration gradient will form along the axis of diffusion. In the next issue of Nature where Crick published his model, an embryologist commented on his unusual proposal of considering diffusion as a mechanism for molecule translocation in live systems as follows:

"I should be grateful to Dr. Francis Crick for allowing me a nostalgic look back at these long-discredited concepts which he has now resurrected – or should I say, canonized – with the double halo of his own reputation and some elegant mathematics. There is however one point that he appears to overlook: the extreme rarity with which sheer diffusion processes occur in living systems. (...) A sheet of frozen-dried tissue, extended between source and sink, might fit Dr. Crick's formulae, but – alas – they would fail to differentiate!" [85].

Clearly, at that time, diffusion was not considered an acceptable mechanism *in vivo*. Nowadays, diffusion of proteins and macromolecules in cells is almost a trivial knowledge. Although mathematically validated, and in spite of its wide acceptance, the SDD model which has been derived from the Crick's model has never been experimentally tested. Since the identification of the Bcd morphogen in 1988 [100], an essential activator of cellular differentiation in the developing embryo of the fruit fly *Drosophila melanogaster*, only one experimental attempt at testing the validity of the SDD has been documented [108]. This attempt failed to detect the most important process in the gradient formation, the fast diffusion of Bcd in the cytoplasm. We have shown here that this was simply because of the wrong choice of technique, namely confocal FRAP.

In this thesis, I employed both FRAP and FCS to study the fraction of mobile Bcd, and more importantly, to detect any possible freely diffusing populations of the protein in the nuclei and the cytoplasm of the *Drosophila* embryo. FRAP confirmed that Bcd is mobile throughout the nuclei with no permanent immobility detected. On the other hand, FCS clearly demonstrated that the majority of Bcd is freely diffusing throughout the embryo with on average $D \sim 4 \ \mu m^2/s$. Thus

38 years after diffusion was proposed as the essential cause for morphogen gradient formation, we have been able to detect the diffusion of a morphogen, Bcd. The highly dynamic behavior of Bcd in the cytoplasm is consistent with the SDD model.

In the embryos' nuclei, since the most important biological function of Bcd is activating gene translation, we also expected to find a considerable fraction of the protein with high mobility, as this is necessary to ensure a high efficiency of the Bcd exchange on the DNA. Indeed, we found that the majority of Bcd was also undergoing diffusion in the nuclei. The presence of a slow nuclear population of Bcd, consistent with its role as a transcription factor transient binding to the DNA, was detected as well.

Finally, we note that the second "D" in the SDD model (Degradation) remains a mysterious process. It has not yet been resolved whether degradation of the Bcd protein happens in the nucleus or in the cytoplasm. In order for us to identify the localization of the degradation process and to understand the actual mechanisms behind it, more work is still needed. The results of both N&B analysis and FCS indicated that the nuclear and cytoplasmic environments in *Drosophila* embryos are different. This was inferred from probing different fluorescence blinking photophysical properties of EGFP in these compartments. This could be indicative of nuclear degradation process as oppose to cytoplasmic. The higher molecular brightness of EGFP in the nucleus could be due to its exposure to more basic nuclear compartments, due to "cooler" nuclear microdomains, or due to other factors like different viscosity or nuclear ionic strength which could asses the degradation process. The fact that nuclear Bcd disappears before the nuclear envelope does could support this view (Work in progress).

Part 4   Summary

This thesis focuses on studying the distribution and mobility of two different nuclear proteins, Ran and Bicoid (Bcd), each in a different type of live cells, HeLa cells and early *Drosophila melanogaster* embryos, respectively. Both studies were done in an attempt to reveal the origins of the large concentration gradients formed by these proteins at the level of a single cell, and to shed light on the biological processes they are involved in. Ran, the key regulator of nucleocytoplasmic transport in eukaryotic cells [45], accumulates in interphase nuclei forming a concentration gradient across the nuclear envelope in spite of its small molecular weight [53]. Although this striking localization is clearly related to the function of this protein as an orchestrator of nuclear transport, little was known about the dynamical mechanisms involved in establishing such localization. On the other hand, Bcd, an essential activator of cellular differentiation along the anterior-posterior axis of early *Drosophila melanogaster* embryos [78], exhibits two forms of concentration gradients. Like Ran, this protein is predominantly nuclear, and forms a nuclear-to-cytoplasmic concentration gradient [100]. More importantly, the Bcd protein exhibits a clear exponential concentration gradient along the anterior-posterior axis of the embryo in the early developmental stages, with its high amplitude at the anterior side [100]. This gradient was proved to be crucial in early development and cellular differentiation in a concentration dependent manner [9], yet the mechanism by which it is formed is still controversial.

In the two separate studies in this thesis, several complementary fluorescence techniques were employed to investigate the distributions and the mobility of fluorescent versions of the two proteins of interest, EYFP-Ran and Bcd-EGFP, in the nuclear and cytoplasmic compartments of their systems. Fluorescence Recovery after Photobleaching (FRAP), Fluorescence Correlation Spectoscopy (FCS), Scanning FCS (SFCS), Molecule Number and Brightness (N&B) Analysis and Raster-Image Correlation Spectoscopy (RICS) were used for the Ran project, while FRAP, FCS and N&B analysis were used for the Bcd project.

The proof that both proteins were highly dynamic in their respective biological systems was one of the major results I obtained. No permanent immobility was detected for either protein according to FRAP experiments. According to FCS experiments, the majority of both proteins

were freely diffusing in the cytoplasm (~70-90%) but with a small population that exhibited dramatically slower motion. The slow cytoplasmic population could be related to either minor complex formation or to transient binding of either protein to cytoplasmic structures. The freely diffusive behavior of cytoplasmic Ran (90%) is consistent with its lack of binding partners in that compartment. Capturing a major cytoplasmic diffusive population of the protein Bcd (70%) is a groundbreaking result, making us the first to validate the most widely and commonly used morphogenetic gradient formation model (the SDD model). In the nucleus of HeLa cells, 30% of Ran was undergoing a very slow motion, probably related to the formation of big protein complexes by Ran. This experimental result is consistent with the large number of RanGTP binding partners found in the nucleus. In the nuclei of early *Drosophila* embryos, 35% of the Bcd population underwent transient binding, probably with DNA as this protein acts as a transcription factor. In both cases, the rest of the proteins were freely diffusing. The dynamic behavior of both proteins in the nuclei of their systems is hardly surprising and is consistent with their biological functions and with the new highly dynamic view of most nuclear proteins studied recently [12, 15]. The localization and dynamics of Ran on the nuclear envelope was of interest to us. A residence time of ~20 ms was measured for Ran on the nuclear envelope, with ~200 copies of Ran present there at all times. The long residence time in comparison to that of other transport factors and the high concentration of the protein at the nuclear envelope allow us to propose that cargo association and dissociation happens at the interface between the nucleus and the cytoplasm, the NPC.

BIBLIOGRAPHY

1. Shapiro, P., *Ras-MAP Kinase Signaling Pathways and Control of Cell Proliferation: Relevance to Cancer Therapy.* Crit Rev Clin Lab Sci, 2002. 39: p. 285-330.

2. Downward, J., *Targeting Ras Signalling Pathways in Cancer Therapy.* Nature Reviews, 2002. 3: p. 11-22.

3. Er, E., et al., *Mitochondria as the Target of the Pro-apoptotic Protein Bax.* Biochimica et Biophysica Acta, 2006. 1757: p. 1301-11.

4. Adams, J.M. and S. Cory, *Life-or-Death Decisions by the Bcl-2 Protein Family.* Trends in Biochemical Sciences, 2001. 26: p. 61-6.

5. Gorlich, D. and U. Kutay, *Transport between the Cell Nucleus and the Cytoplasm.* Annu. Rev. Cell Dev. Biol, 1999. 15: p. 607-60.

6. Malumbres, M. and M. Barbacid, *To Cycle or not to Cycle: a Critical Decision in Cancer.* Nature Reviews, 2001. 1: p. 222-31.

7. Chen, K. and N. Rajewsky, *The Evolution of GENE Regulation by Transcription Factors and MicroRNAs.* Nature Reviews, 2007. 8: p. 93-103.

8. Gerthoffer, W.T., *Mechanisms of Vascular Smooth Muscle Cell Migration.* Circ. Res., 2007. 100: p. 607-21.

9. Driever, W. and C. Nusslein-Volhard, *The Bicoid Protein Determines Position in the Drosophila Embryo in a Concentration-Dependent Manner.* Cell, 1988b. 54: p. 95-104.

10. Nelson, P., *Biological Physics: Energy, Information, Life,* ed. S.F. Brennan. Vol. 1. 2004, New York: W. H. Freeman and Company. 598.

11. Banks, D.S. and C. Fradin, *Anomalous Diffusion of Proteins due to Molecular Crowding.* Biophysical Journal, 2005. 89(5): p. 2960-71.

12. Mikuni, S., M. Tamura, and M. Kinjo, *Analysis of Intranuclear Binding Process of Glucocorticoid Receptor using Fluorescence Correlation Spectroscopy.* FEBS Letters, 2007. 581: p. 389-93.

13. Yeung, C., M. Shtrahman, and X. Wu, *Stick-and-Diffuse and Caged Diffusion: a Comparison of Two Models of Synaptic Vesicle Dynamics.* Biophysical Journal, 2007. 92: p. 2271-80.

14. Lippincott-Schwartz, J., E. Snapp, and A. Kenworthy, *Studying protein Dynamics in Living Cells.* Nature, 2001. 2: p. 444-56.

15. Phair, R.D. and T. Misteli, *High Mobility of Proteins in the Mammalian Cell Nucleus.* Nature, 2000. 404: p. 604-9.

16. Hager, G.L., C. Elbi, and M. Becker, *Protein Dynamics in the Nuclear Compartment.* Current Opinion in Genetics & Development, 2002. 12: p. 137-41.

17. Belmont, A., *Dynamics of Chromatin, Proteins, and Bodies Within the Cell Nucleus.* Current Opinion in Cell Biology, 2003. 15: p. 304-10.

18. Beaudouin, J., et al., *Dissecting the Contribution of Diffusion and Interactions to the Mobility of Nuclear Proteins.* Biophysical Journal, 2006. 90: p. 1878-1894.

19. *Handbook of Biomedical Fluorescence*, ed. M.-A. Mycek and B.W. Poque. 2003, New York: Marcel Dekker Inc.

20. Resch-Genger, U., et al., *Quantum Dots Versus Organic Dyes as Fluorescent Lables.* Nature Methods, 2008. 5: p. 763-75.

21. Tsien, R.Y., *The Green Fluorescent Protein.* Annu. Rev. Biochem, 1998. 67: p. 509-44.

22. *Green Fluorescent Proteins: Properties, Applications and Protocols*, ed. M. Chalfie and S.R. Kain. 1998, NJ: Wiley-Liss Inc.

23. Haupts, U., et al., *Dynamics of Fluorescence Fluctuations in Green Fluorescent Protein Observed by Fluorescence Correlation Spectroscopy.* PNAS, 1998. 95: p. 13573-8.

24. Henis, Y.I., B. Rotblat, and Y. Kloog, *FRAP Beam-Size Analysis to Measure Palmitoylation-Dependent Membrane Association Dynamics and Microdomain Partitioning of Ras Proteins.* Methods, 2006. 40: p. 183-90.

25. Sekar, R.B. and A. Periasamy, *Fluorescence Resonance Energy Transfer (FRET) Microscopy Imaging of Live Cell Protein Localization.* The Journal of Cell Biology, 2003. 160: p. 629-33.

26. Ramedios, C.G., M. Miki, and J.A. Barden, *Fluorescence Resonance Energy Transfere Measurements of Distances in Activated Myosin. A Critical Evolution.* J Muscle Res Cell Motil, 1987. 8: p. 97-117.

27. Bastiaens, P.I.H. and A. Squire, *Fluorescence Lifetime Imaging Microscopy: Spatial Resolution of Biochemical Processes in the Cell.* Trends in Cell Biology, 1999. 9: p. 48-52.

28. Digman, M.A., et al., *The Phasor Approach to Fluorescence Lifetime Imaging Analysis.* Biophysical Journal, 2008. 94: p. L14-L16.

29. Khatchadourian, R., et al., *Fluorescence Intensity and Intermittency as Tools for following Dopamine Bioconjugate Processing in Living Cells.* Journal of Biomedicine and Biotechnology, 2007. 10: p. 1155-65.

30. Kolin, D.L. and P.W. Wiseman, *Advances in Image Correlation Spectroscopy: Measuring Number Densities, Aggregation States, and Dynamics of Fluorescently Labeled Macromolecules in Cells.* Cell Biochem Biophys, 2007.

31. Petersen, N.O., et al., *Quantitation of Membrane Receptor Distributions by Image Correlation Spectroscopy: Concept and Application.* Biophysical Journal, 1993. 65: p. 1135-1146.

32. Digman, M.A., et al., *Fluctuation Correlation Spectroscopy with a Laser-Scanning Microscope: Exploiting the Hidden Time Structure.* Biophysical Journal, 2005. 88(5): p. L33-L36.

33. Digman, M.A., et al., *Measuring Fast Dynamics in Solutions and Cells with a Laser Scanning Microscope.* Biophysical Journal, 2005. 89: p. 1317-27.

34.   Brown, C.M., et al., *Raster Image Correlation Spectroscopy (RICS) for Measuring Fast Protein Dynamics and Concentrations with a Commercial Laser Scanning Confocal Microscope.* J Microsc, 2008. 229: p. 78-91.

35.   Dalal, R.B., et al., *Determination of Particle Number and Brightness Using a Laser Scanning Confocal Microscope Operating in the Analog Mode.* Microscopy Research and Technigue, 2007. 71(1): p. 69-81.

36.   Qian, H. and E.L. Elson, *Distribution of Molecular Aggregation by Analysis of Fluctuation Moments.* PNAS, 1990. 87(14): p. 5479-83.

37.   Niv, H., et al., *Membrane Interactions of a Constitutively Active GFP-Ki-Ras 4B and Their Role in Signaling.* The Journal of Biological Chemistry, 1999. 274: p. 1606-13.

38.   Borejdo, J., *Motion of Myosin Fragments During Actin-Activated ATPase: Fluorescence Correlation Spectoscopy Study.* Biopolymers, 1979. 18: p. 2807-20.

39.   Gosch, M., et al., *Hydrodynamic Flow Profiling in Microchannel Structures by Single Molecule Fluorescence Correlation Spectroscopy.* Anal Chem, 2000. 72: p. 3260-5.

40.   Rigler, R. and E.S. Elson, *Fluorescence Correlation Spectroscopy: Theory and Applications,* ed. F.P. Schafer, W. Zinth, and J.P. Toennies. 2001, Berlin: Springer.

41.   Wachsmuth, M., W. Waldeck, and J. Langowski, *Anomalous Diffusion of Fluorescent Probes Inside Living Cell Nuclei Investigated by Spatially-Resolved Fluorescence Correlation Spectroscopy.* Journal of Molecular Biology, 2000. 289: p. 677-89.

42.   Nemergut, M.E., et al., *Chromatin Docking and Exchange Activity Enhancement of RCC1 by Histones H2A and H2B.* Science, 2001. 292: p. 1540-3.

43.   Chen, T., et al., *N-Terminal Alpha-Methylation of RCC1 is Necessary for Stable Chromatin Association and Normal Mitosis.* Nat Cell Biol, 2007. 9: p. 596-603.

44.   Joseph, J., et al., *SUMO-1 Targets RanGAP1 to Kinetochores and Mitotic Spindles.* J Cell Biol, 2002. 156: p. 595-602.

45.   Weis, K., *Regulating Access to the Genome: Nucleocytoplasmic Transport Throughout the Cell Cycle.* Cell, 2003. 112: p. 441-51.

46.   Hetzer, M., O.J. Gruss, and I.W. Mattaj, *The Ran GTPase as a Marker of Chromosome Position in Spindle Formation and Nuclear Envelope Assembly.* Nat Cell Biol, 2002. 4: p. E177-84.

47.   Lee, S.J., et al., *Structural Basis for Nuclear Import Complex Dissociation by RanGTP.* Nature, 2005. 435: p. 693-6.

48.   Fried, H. and U. Kutay, *Nucleocytoplasmic Transport: Taking and Inventory.* Cell Mol Life Sci, 2003. 60: p. 1659-88.

49.   Ribbeck, K., et al., *NTF2 Mediates Nuclear Import of Ran.* Embo J, 1998. 17: p. 6587-98.

50. Nakielny, S. and G. Dreyfuss, *Transport of Proteins and RNAs In and Out of the Nucleus.* Cell, 1999. 99: p. 677-90.

51. Smith, A.E., et al., *Systems Analysis of Ran Transport.* Science, 2002. 295: p. 488-91.

52. Gorlich, D., M. J.Seewald, and K. Ribbeck, *Characterization of Ran-driven cargo transport and the RanGTPase system by kinetic measurements and computer simulation.* The EMBO Journal, 2003. 22(5): p. 1088-1100.

53. Ren, M., et al., *Ran/TC4: A Small Nuclear GTP-binding Protein That Regulates DNA Synthesis.* The Journal of Cell Biology, 1993. 120(2): p. 313-23.

54. Bischoff, F.R. and H. Ponstingl, *Mitotic Regulator Protein RCC1 is Complexed with a Nuclear ras-related Polypeptide.* PNAS, 1991. 88: p. 10830-34.

55. Hinkle, B., et al., *Chromosomal Association of Ran during Meiotic and mitotic divisions.* Journal of Cell Science, 2002. 115: p. 4685-93.

56. Kelley, J.B. and B.M. Paschal, *Hyperosmotic Stress Signaling to the Nucleus Disrupts the Ran Gradient and the Production of RanGTP.* Mol Biol Cell, 2007.

57. Paradise, A., et al., *Significant Proportions of Nuclear Transport Proteins with Reduced Intracellular Mobilities Resolved by Fluorescence Correlation Spectroscopy.* J Mol Biol, 2007. 365: p. 50-65.

58. Lounsbury, K.M., A.L. Beddow, and I.G. Macara, *A Family of proteins That Stabilize the Ran/TC4 GTPase in Its GTP-bound Conformation.* The Journal of Biological Chemistry, 1994. 269(15): p. 11285-90.

59. Gorlich, D., et al., *Identification of Different Roles for RanGDP and RanGTP in Nuclear Protein Import.* EMBO J, 1996. 15(20): p. 5584-94.

60. Gorlich, D., et al., *A Novel Class of RanGTP Binding Proteins.* The Journal of Cell Biology, 1997. 138(1): p. 65-80.

61. Ohtsubo, M., H. Okazaki, and T. Nishimoto, *The RCC1 Protein, a Regulator for the Onset of Chromosome Condensation Locates in the Nucleus and Binds to DNA.* The Journal of Cell Biology, 1989. 109: p. 1389-97.

62. Bilbao-Cortes, D., et al., *Ran Binds to Chromatin by Two Distinct Mechanisms.* Curr Biol, 2002. 12: p. 1151-6.

63. Moore, M.S., *Ran and nuclear transport.* The Journal of Biological Chemistry, 1998. 273(36): p. 22857-60.

64. Rout, M.P., et al., *The Yeast Nuclear Pore Complex: Composition, Architecture, and Transport Mechanism.* J Cell Biol, 2000. 148: p. 635-51.

65. Schwille, P., J. Korlack, and W. Webb, *Fluorescence Correlation Spectroscopy with Single-Molecule Sensitivity on Cell and Model Membranes.* Cytometry, 1999. 36: p. 176-82.

66. Kim, S.A., K.G. Heinze, and P. Schwille, *Fluorescence Correlation Spectroscopy in Living Cells.* Nat. Methods, 2007. 4: p. 963-73.

67. Martin, B.R., et al., *Mammalian Cell-Based Optimization of the Biarsenical-Binding Tetracystine Motif for Improved Fluorescence and Affinity.* Nat. Biotechnol., 2005. 23: p. 1308-14.

68. Delon, A., et al., *Continuous Photobleaching in Vesicles and Living Cells: A Measure of Diffusion and Compartmentation.* Biophysical Journal, 2006. 90: p. 2548-62.

69. Keryer, G., et al., *Part of Ran is Associated with AKAP450 at the Centrosome: Involvement in Microtubule-Organizing Activity.* Mol. Biol. Cell., 2003. 14: p. 4260-71.

70. Klebe, C., et al., *The Kinetic Mechanism of Ran-Nucleotide Exchange Catalyzed by RCC1.* Biochemistry, 1995. 34: p. 12543-52.

71. Yang, W., J. Gelles, and S.M. Musser, *Imaging of Single-Molecule Translocation through Nuclear Pore Complexes.* PNAS USA, 2004. 101: p. 12887-92.

72. Ribbeck, K. and D. Gorlich, *Kinetic Analysis of Translocation Through Nuclear Pore Complexes.* EMBO J, 2001. 20: p. 1320-30.

73. Kubitscheck, U., et al., *Nuclear Transport of Single Molecules: Dwell Times at the Nuclear Pore Complex.* J Cell Biol, 2005. 174: p. 951-61.

74. Yang, W. and S.M. Musser, *Nuclear Import Time and Transport Efficiency Depend on Importin B Concentration.* JCB, 2006. 174(7): p. 951-61.

75. Lindsay, M.E., et al., *Npap60/Nup50 is a Tri-stable Switch that Stimulates Importin-alpha:beta-Mediated Nuclear Protein Import.* Cell, 2002. 110(3): p. 349-60.

76. Yaseen, N.R. and G. Blobel, *Two Distinct Classes of Ran-Binding Sites on the Nucleoporin Nup-358.* PNAS USA, 1999. 96: p. 5516-21.

77. yokoyama, N., et al., *A Giant Nucleopore Portein that Binds Ran/TC4.* Nature, 1995. 376: p. 184-8.

78. Ephrussi, A. and D. St.Johnston, *Seeing is Believing: The Bicoid Morphogen Gradient Matures.* Cell, 2004. 116: p. 143-52.

79. St Johnston, D. and C. Nusslein-Volhard, *The Origin of Pattern and Polarity in the Drosophila Embryo.* Cell, 1992. 68: p. 201-19.

80. Crick, F., *Diffusion in Embryogenesis.* Nature, 1970. 225: p. 420-2.

81. Wolpert, L., *Positional Information and the Spatial Pattern of Cellular Differentiation.* Journal of Theoretical Biology, 1969. 25(1): p. 1-47.

82. Wolpert, L., *One Hundred Years of Positional Information.* Trends Genet, 1996. 12: p. 359-64.

83. Child, C.M., *Individuality in Organisms.* 1915, Chicago: The University of Chicago Press. x+213.

84. Morgan, T.H., *Regeneration of Proportionate Structures in Stentor.* Biol Bull, 1901. 2: p. 311-28.

85. Deuchar, E.M., *Diffusion in Embryogenesis.* Nature, 1970. 225: p. 671.

86. Arias, A.M., *Drosophila melanogaster and the Development of Biology in the 20th Century*, in *Methods in Molecular Biology*, C. Dahmann, Editor. 2007, Springer Science & Business Media: NJ.

87. Akam, M., *The Molecular Basis for Metameric Pattern in the Drosophila Embryo.* Development, 1987. 101: p. 1-22.

88.   Nusslein-Volhard, C. and E. Weischaus, *Mutations Affecting Segment number and Polarity in Drosophila.* Nature, 1980. 287: p. 795-801.

89.   Nusslein-Volhard, C., E. Wieschaus, and H. Kluding, *Mutations Affecting the Pattern of the Larval Cuticle in Drosophila Melanogaster. I. Zygotic Loci on the Second Chromosome.* Wilheim Roux Arch Dev Biol, 1984. 193: p. 267-82.

90.   Nusslein-Volhard, C., *Genetic Analysis of Pattern Formation in the Ebmryo of Drosophila Melanogaster. Characterization of the Maternal-Effect Mutant Bicaudal.* Rouxs Arch. Dev. Biol., 1977a. 183: p. 249-68.

91.   Nusslein-Volhard, C., et al., *A Dorsal-Ventral Shift of Embryonic primordia in a New Maternal-Effect Mutant of Drosophila.* Nature, 1980. 283: p. 474-6.

92.   Schupbach, T. and E. Weischaus, *Maternal-Effect Mutations Altering the Anterior-Posterior Pattern of the Drosophila Embryo.* Rouxs Arch. Dev. Biol., 1986. 195: p. 302-17.

93.   Nusslein-Volhard, C., H.G. Frohnhofer, and R. Lehmann, *Determination of Anteroposterior Polarity in Drosophila.* Science, 1987. 238: p. 1675-1681.

94.   Frohnhofer, H.G. and C. Nusslein-Volhard, *Organization of Anterior Pattern in The Drosophila Embryo by the Maternal Gene Bicoid.* Nature, 1986. 324: p. 120-5.

95.   Frohnhofer, H.G. and C. Nusslein-Volhard, *Maternal Genes Required for the Anterior Localization of Bicoid Activity in the Embryo of Drosophila.* Genes Dev, 1987. 1: p. 880-90.

96.   Frohnhofer, H.G., R. Lehmann, and C. Nusslein-Volhard, *Manipulating the Anteroposterior Pattern of the Drosophila Embryo.* J Ambryol Exp Morph, 1986. 97: p. 169-79.

97.   Anderson, K.V. and C. Nusslein-Volhard, *Information for the Dorsal-Ventral Pattern of the Drosophila Embryo is Stored as Maternal mRNA.* Nature, 1984. 311: p. 223-7.

98.   Mohler, J. and E.F. Wieschaus, *Dominant Maternal-Effect Mutations of Drosophila Melanogaster Causing the Production of Double-Abdomen Embryos.* Genetics, 1986. 112: p. 803-22.

99.   Nusslein-Volhard, C., *A Rapid Method for Screening Eggs from Single Drosophila Females.* Drosophila Inform Serv, 1977b. 52: p. 166.

100. Driever, W. and C. Nusslein-Volhard, *A Gradient of Bicoid Protein in Drosophila Embryos.* Cell, 1988a. 54: p. 83-93.

101. Berleth, T., et al., *The Role of Localization of Bicoid RNA in Organizing the Anterior Pattern of the Drosophila Embryo.* EMBO J, 1988. 7(6): p. 1749-56.

102. Frigerio, G., et al., *Structure of the Segmentation Gene Paired and the Drosophila PRD Gene Set as Part of a Gene Network.* Cell, 1986. 47: p. 735-46.

103. Driever, W. and C. Nusslein-Volhard, *The Bicoid Protein is a Positive Regulator of Hunchback Transcription in the Early Drosophila Embryo.* Nature, 1989a. 337: p. 138-43.

104. Driever, W. and C. Nusslein-Volhard, *Determination of Spatial Domains of Zygotic Gene Expression in the Drosophila Embryo by the Affinity of Binding Sites for the Bicoid Morphogen.* Nature, 1989b. 340: p. 363-7.

105.   Gao, Q. and R. Finkelstein, *Targeting Gene Expression to the Head: The Drosophila Orthodenticle Gene is a Direct Target of the Bicoid Morphogen.* Development, 1998. 125: p. 4185-93.

106.   Baird-Titus, J.M., et al., *The Solution Structure of the Native k50 Bicoid Homeodomain Bound to the Consensus TAATCC DNA-Binding Site.* J. Mol. Biol, 2006. 356: p. 1137-51.

107.   Lewis, J., J. Slack, and L. Wolpert, *Thresholds in Development.* J Theor Biol, 1977. 65(3): p. 579-90.

108.   Gregor, T., et al., *Stability and Nuclear Dynamics of the Bicoid Morphogen Gradient.* Cell, 2007. 130(1): p. 141-152.

109.   Houchmandzadeh, B., E. Wieschaus, and S. Leibler, *Precise Domain Specification in the Developing Drosophila Embryo.* Physical Review, 2005. 72: p. 061920.

110.   Houchmandzadeh, B., E. Wieschaus, and S. Leibler, *Establishment of Developmental Precision and Proportions in the Early Drosophila Embryo.* Nature, 2002. 415: p. 798-802.

111.   Gregor, T., A.P. McGregor, and E.F. Wieschaus, *Shape and function of the Bicoid Morphogen Gradient in Dipteran Species with Different Sized Embryos.* Developmental Biology, 2008. 316: p. 350-358.

112.   Wojcieszyn, J.W., et al., *Diffusion of Injected Macromolecules within the Cytoplasm of Living Cells.* PNAS USA, 1981. 78: p. 4407-10.

113.   Gregor, T., et al., *Probing the Limits to Positional Information.* Cell, 2007. 130(1): p. 153-164.

114.   Foe, V.E. and B.M. Alberts, *Studies of Nuclear and Cytoplasmic Behaviour During the Five Mitotic Cycles that Precede Gastrulation in Drosophila Embryogenesis.* J Cell Sci, 1983. 61: p. 31-70.

115.   Bachir, A.I., et al., *A Guide to Accurate Measurement of Diffusion Using Fluorescence Correlation Techniques with Blinking Quantum Dot Nanoparticles Labels.* The Journal of Chemical Physics, 2008. 128: p. 225105.

116.   Chen, Y., L.-N. Wei, and J.D. Muller, *Probing Protein Oligomerization in Living Cells with Fluorescence Fluctuation Spectroscopy.* PNAS, 2003. 100: p. 15492-7.

117.   Wong, F., et al., *A Molecular Thermometer Based on Fluorescent Protein Blinking.* J Am Chem Soc, 2007. 129: p. 10302-10303.

118.   Bader, N., T. Jung, and T. Grune, *The Proteasome and Its Role in Nuclear Protein Maintenance.* Experimental Gerontology, 2007. 42: p. 864-70.

119.   Rivett, A.P. and E. Knecht, *Electron Microscopic Localization of the Multicatalytic Proteinase Complex in Rat Liver and Cultured Cells.* J. Histochem. Cytochem., 1992. 40: p. 1165-72.

120.   Rocheleau, J.V. and D.W. Piston, *Two-Photon Excitation Microscopy For the Study of Living Cells and Tissues.* Current Protocols in Cell Biology, 2003. 4.11(1-15).

121.   Sun, C., et al., *Single-Molecule Measurements of Importin Alpha/Cargo Complex Dissociation at the Nuclear Pore.* PNAS USA, 2008. 105: p. 8613-9.

Appendix A

Maple Code for the Stick-and-Diffuse Model

```
> restart:

fd:=fopen(`3D_Wu_all3.txt`,WRITE,TEXT):
fr:=fopen(`3D_Wu_final.txt`,WRITE,TEXT):
ft:=readdata(`ACF_t_RanN.txt`,float):
fn:=readdata(`ACF_RanN.txt`,float):


m:=262:
#tauD:=1.4:
#tauU:=7:
#tauB:=8:
#Num:=1.3:
S:=6:

for Num from 1.2 by 1.2 to 1.2 do

 for tauD from 1.3 by 1.3 to 1.3 do

  for tauU from 82 by 82 to 82 do

   for tauB from 32 by 32 to 32 do

    for tBlnk from 0.16 by 0.16 to 0.16 do

     for BR from 0.17 by 0.17 to 0.17 do

      cnt:=0:
 for i from 1 by 1 to m do
  t:=ft[i];

 A1:=tauB*exp(-t/tauB)/(tauU+tauB):
 A2:=(tauU*exp(-t/tauU)/((tauU+tauB)*(1+t/tauD)))*(1/sqrt(1+(1/S^2)*(t/tauD))):
        count:=0:
    for n from 1 by 1 to 7 do
```

```
sumt:=(1/((tauU+tauB)*(n-1)!*n!))*evalf(int((exp(-(t-x)/tauB-
x/tauU)/(1+x/tauD))*(1/sqrt(1+(1/S^2)*(x/tauD)))*(2*n+(x/tauB+(t-x)/tauU))*(x*(t-
x)/(tauU*tauB))^(n-1),x=0..t)):


         count:=count+sumt:
                       end do:

     A3:=count:
     Blink:=1+(BR/(1-BR))*exp(-t/tBlnk):


     ACF:=(1/Num)*(A1+A2+A3)*Blink:
     Res:=(fn[i]-ACF)^2:
     cnt:=cnt+Res:

     #print(t,ACF,Res):



     fprintf(fr, `%g %g %g\n`, t, ACF, Res):

                   end do:

     SumRes:=cnt:
     fprintf(fd, `%g %g %g %g %g %g %g\n`, Num, tauD, tBlnk, BR, tauU, tauB,
SumRes):

                 end do:
                   end do:
                     end do:
                       end do:
                        end do:
                          end do:

fclose(fd);
fclose(fr);
```